An Investigation of Plastic Fracture in Aluminum Alloys

by
J. R. Low, Jr.,
R. H. VanStone,
and
R. H. Merchant

TR-#2

METALS RESEARCH LABORATORY
CARNEGIE INSTITUTE OF TECHNOLOGY

Carnegie-Mellon University

PITTSBURGH, PENNSYLVANIA

National Aeronautics and Space Administration
Research Grant NGR 39-087-003

An Investigation of Plastic Fracture in Aluminum Alloys

by
J. R. Low, Jr.,
R. H. VanStone,
and
R. H. Merchant

TR-#2

Metallurgy and Materials Science
Carnegie-Mellon University
Pittsburgh, Pennsylvania 15213

NASA Technical Report No. 2

May 1972

This investigation was made possible by a Research Grant from the National Aeronautics and Space Administration

INTRODUCTION

The brittle fracture of many high-strength alloys such as, steel, titanium, and aluminum have been shown in many cases to occur by a process called plastic fracture[1]. Plastic fracture is the mode of fracture where microscopic voids form at impurity particles, then grow and coalesce to cause the final rupture. A previous segment of this investigation[2] assessed the role played by impurity particles in 2014 T6 aluminum alloy. To further understand the role played by impurities, four other aluminum alloys have been investigated: 2024-T851, 2124-T851, 7075-T7351 and 7079-T651. Fractography, quantitative metallography, and microprobe studies have helped assess the roles of various particles. This is a progress report of that investigation.

MATERIALS

In the study, five aluminum alloys were investigated, all of which were precipitation hardened alloys with various thermal-mechanical treatments. Three of the alloys, 2014-T6, 2024-T851, and 2124-T851, are primarily Al-Cu alloys while the others, 7075-T7351 and 7079-T651, are primarily Al-Mg-Zn alloys. Table I lists chemical specifications, check analyses, and temper designations for the alloys. All the alloys, excluding 2124-T851, are commercial alloys. Alloy 2124-T851 has the same chemical specification as 2024-T851 except for reduced levels of silicon and iron as reflected in the check analyses.

The 2014-T6 material was the same as that used in the investigation of Tanaka, Pampillo, and Low[2]. The 2024-T851, 7075-T7351, and

TABLE I

Composition and Heat Treatment of Aluminum Alloys

(Weight Percent)

Alloy		Si	Fe	Cu	Zn	Mg	Mn	Cr	Ti	V	Al
2014-T6[1]	Specification	0.5/1.2	0.7 Max	3.9/5.0	0.25 Max	0.2/0.8	0.4/1.2	0.10 Max	0.15 Max	-	Bal.
	Analysis	0.83	0.20	4.67	-	0.51	0.73	-	-	-	-
2024-T851[2]	Specification	0.5 Max	0.5 Max	3.8/4.9	0.25 Max	1.2/1.8	0.3/0.9	0.10 Max	-	-	Bal.
	Analysis	0.17	0.50	4.2	0.077	1.52	0.59	0.018	0.05	0.018	-
2124-T851[2]	Specification	0.2 Max	0.3 Max	3.8/4.9	0.25 Max	1.2/1.8	0.3/0.9	0.10 Max	-	-	Bal.
	Analysis	0.04	0.05	4.11	0.02	1.41	0.61	0.00+	0.02	0.00+	-
7075-T7351[3]	Specification	0.5 Max	0.7 Max	1.2/2.0	5.1/6.1	2.1/2.9	0.3 Max	0.18/0.40	0.2 Max	-	Bal.
	Analysis	0.098	0.22	1.65	5.50	2.48	0.033	0.21	0.033	0.008	-
7079-T651[4]	Specification	0.3 Max	0.4 Max	0.4/0.8	3.8/4.8	2.9/3.7	0.1/0.3	0.1/0.25	0.1 Max	-	Bal.
	Analysis	0.11	0.19	0.76	4.60	3.30	0.23	0.17	0.024	0.009	-

Typical Heat Treatments: (Aluminum Standards and Data 1970-71, Aluminum Association, New York)

1. 2014-T6 - Solution treatment at 935°F, quenched, age 18 hrs. at 320°F.
2. 2024-T851, 2124-T851 - Solution treatment at 920°F, quenched, stress-relieved by stretching, age 12 hrs. at 375°F.
3. 7075-T7351 - Solution treatment at 900°F, quenched, stress-relieved by stretching, age 6-8 hrs. at 225°F, followed by 24-30 hrs. age at 325°F.
4. 7079-T651 - Solution treatment at 830°F., stress-relieved by stretching, age 5 days at room temperature, followed by 48 hour age at 240°F.

7079-T651 material was supplied by J. G. Kaufman of Alcoa Research Laboratories in the form of three point bend, plane strain fracture toughness specimens. H. Y. Hunsicker of Alcoa Research Laboratories supplied two, three-inch thick test blocks of 2124-T851.

For this study, both tensile tests and plane strain fracture toughness tests were conducted. The K_{Ic} fracture toughness values for 2024-T851, 7075-T7351, and 7079-T651 were those reported by J. G. Kaufman[3]. The K_{Ic} fracture toughness tests on 2014-T6 and 2124-T851 were performed at the NASA Lewis Research Center by W. F. Brown and M. H. Jones.

Table II shows the 0.2% offset yield stress (σ_o), room temperature K_{Ic} values, and relative toughness (K_{Ic}/σ_o). Also shown are the strength coefficient (A) and the strain hardening exponent (n) from the flow curve least square fit to $\sigma = A\epsilon^n$. In Table II, the symbols in parenthesis represent the specimen orientation where R is the principal rolling direction, W is the transverse direction, and T is the thickness direction. The tensile tests are characterized by the tensile axis and the fracture toughness tests are characterized by the normal to the fracture plane (or major tensile axis) followed by the direction of crack propagation. With the exception of 2014-T6 and 2124-T851, the fracture planes of both tests are the same. Fracture toughness tests on the RT orientation of 2124-T851 are currently being carried our for comparison with the 2124-T851 tensile behavior and 2024-T851 K_{Ic} value of the same orientation. Note that 2014-T6 and 2024-T851 have virtually the same toughness while 2124-T851, with decreased iron and silicon content, has the same strength as the other 2000 series alloys but a significantly

TABLE II

Mechanical Test Results

Alloy	Yield Stress σ_y (ksi)	K_{Ic} (ksi $\sqrt{in.}$)	K_{Ic}/σ_y ($\sqrt{in.}$)	Flow Curve $\sigma = A\epsilon^n$ A (ksi)	n
2014-T6	63.5 (R)	17.7 ± 0.8 (TW)	0.277	87.1 ± 0.8	0.064 ± 0.003
2024-T851	64.4 (R)	18.8 (RT)	0.292	85.5 ± 0.1	0.051 ± 0.000+
2124-T851	63.3 (R)	23.8 ± 0.6 (TR)	0.378	93.6 ± 1.1	0.074 ± 0.003
7079-T651	73.0 (R)	24.9 (RT)	0.495	110.0 ± 1.0	0.074 ± 0.003
7075-T7351	56.8 (R)	28.1 (RT)	0.341	92.6 ± 1.1	0.097 ± 0.004

improved K_{Ic} fracture toughness from 18.8 to 23.8. The two 7000 series alloys show the usual inverse relation between strength and toughness, and comparison of 2124-T851 and 7079-T651 illustrates that at the same toughness level the 7000 series alloys possess higher strength[1].

FRACTOGRAPHIC STUDY

The fracture surface of each alloy was studied with the two stage plastic-carbon replicas. The replicas were taken from fracture toughness specimens near the point of onset of fast fracture. These alloys, like 2014-T6[2], have fracture surfaces characterized by regions of large and small dimples as illustrated in Figure 1 for 2024-T851. Region A is a region of large dimples surrounded by regions of small dimples as in Region B. The large dimple diameters are on the order of 10 microns and show slip traces known as serpentine glide marks[5]. In their centers there is often a cracked particle such as C which size is on the order of microns. The particles failed by cleavage as shown by the river patterns[4]. When fractographs are viewed in stereo pairs, the regions of small dimples are seen to be at a large angle to the macroscopic plane of crack propagation and connect planes of large dimple clusters. The size of the small dimples is on the order of 0.1 micron. Fractographs for 2124-T851, 7075-T7351, and 7079-T651 are shown in Figures 2, 3, and 4, respectively. Comparisons of these micrographs show that as the toughness is increased, the large dimples become deeper and fracture surface in general deviates more from an ideal plane of crack propagation. It also becomes more difficult to distinguish between regions of large and small dimples due to the increased amount of local plastic

Figure 1 - Fractograph of 2024 T851 with Regions of Large Dimples (A), Regions of Small Dimples (B), and Cracked Particles (C)

Figure 2 - Fractograph of 2124 T851 with Regions of Large Dimples (A), Regions of Small Dimples (B), and Cracked Particles (C)

Figure 3 - Fractograph of 7075 T7351. The Distinction Between Areas of Small and Large Dimples is Very Difficult

Figure 4 - Fractograph of 7079 T651 with Regions of Large Dimples (A), Regions of Small Dimples (B), and Cracked Particles (C)

deformation. In 7075-T7351 (Figure 3), the toughest alloy studied, the edge between a large dimple and an adjacent region of small dimples was more diffuse than in a less tough alloy like 2024-T851 (Figure 1).

The fractographs for all the alloys with the exception of 7075-T7351 were characterized quantitatively. Measurements on the 7075-T7351 micrographs were impossible due to the surface roughness effects. The quantities measured were:

1. Percentage of the area covered by large dimples (A/o LD)
2. Percentage of the area covered by cracked particles (A/o CP)
3. Number of large dimples per unit area
4. Number of cracked particles per unit area
5. Average diameter of large dimples
6. Small dimple spacing in regions of small dimples

To assess void growth, a void growth parameter (VGP) is defined as

$$VGP = \sqrt{(A/o\ LD)/(A/o\ CP)} \qquad \text{Eq.(1)}$$

This would be the same as the ratio of large dimple diameter to the diameter of the cracked particle when each dimple is nucleated by one particle. This is not always the case, but in each dimple there is usually one large cracked particle which probably nucleated the dimple. The fractographic data are shown in Table III and are based on at least five fractographs for each alloy.

FAILURE OF LARGE INCLUSIONS

Optical microscopy and scanning electron microscopy were used to determine the role played by the large (greater than 1 micron) second

TABLE III

Fractographic Data

Feature	2014-T6	2024-T851	2124-T851	7079-T651
Area Covered by Large Dimples (%)	57.5	46.9	64.1	43.6
Area Covered by Cracked Particles (%)	5.4	2.7	3.4	2.1
Number of Large Dimples Per Unit Area ($10^5/cm^2$)	8.0	13.4	8.6	11.1
Number of Cracked Particles Per Unit Area ($10^5/cm^2$)	10.4	18.7	16.3	15.7
Average Diameter of Large Dimples (μ)	9.6	6.7	10.6	7.1
Small Dimple Intercept Distance (μ)	0.78	0.58	0.84	0.48
Void Growth Parameter	3.24	4.17	4.35	4.56

phase particles in the process of plastic fracture. In general, these particles are non-metallic inclusions which form during the freezing of the alloys. As in the investigation of Tanaka, Pampillo, and Low[2], the role the inclusions play was determined by straining flat, 0.1 inch thick tensile specimens and observing polished sections at the midplane of the specimen. In most of these alloys there are more than one kind of second-phase particles so that the particle which fails first can be noted. This was verified by viewing the cross-section in the scanning electron microscope (SEM). Other useful information obtained was the relationship between the number of cracked second-phase particles greater than 2 microns, and the macroscopic deformation state. No particles smaller than 2 microns were observed to crack using the methods of examination described above. The standard deviation of this data is close to 2% in all cases. Each alloy will be discussed in detail.

A. 2014-T6 (as reported by Tanaka, et.al.[2])

This alloy has two types of inclusions, as shown in Figure 5, that can be described as clear gray (C) and dark gray (D). Cracking studies showed that the largest particles cracked first, as shown in Figure 6, but there was no apparent difference in the cracking behavior of the two particles. Figure 7 shows the cracking data as the percentage of particles cracked as a function of plastic elongation. Particles start to crack shortly after yielding.

B. 2024-T851

This alloy has three types of particles, as shown in Figure 8. The light (L) and gray (G) particles were observed to crack at

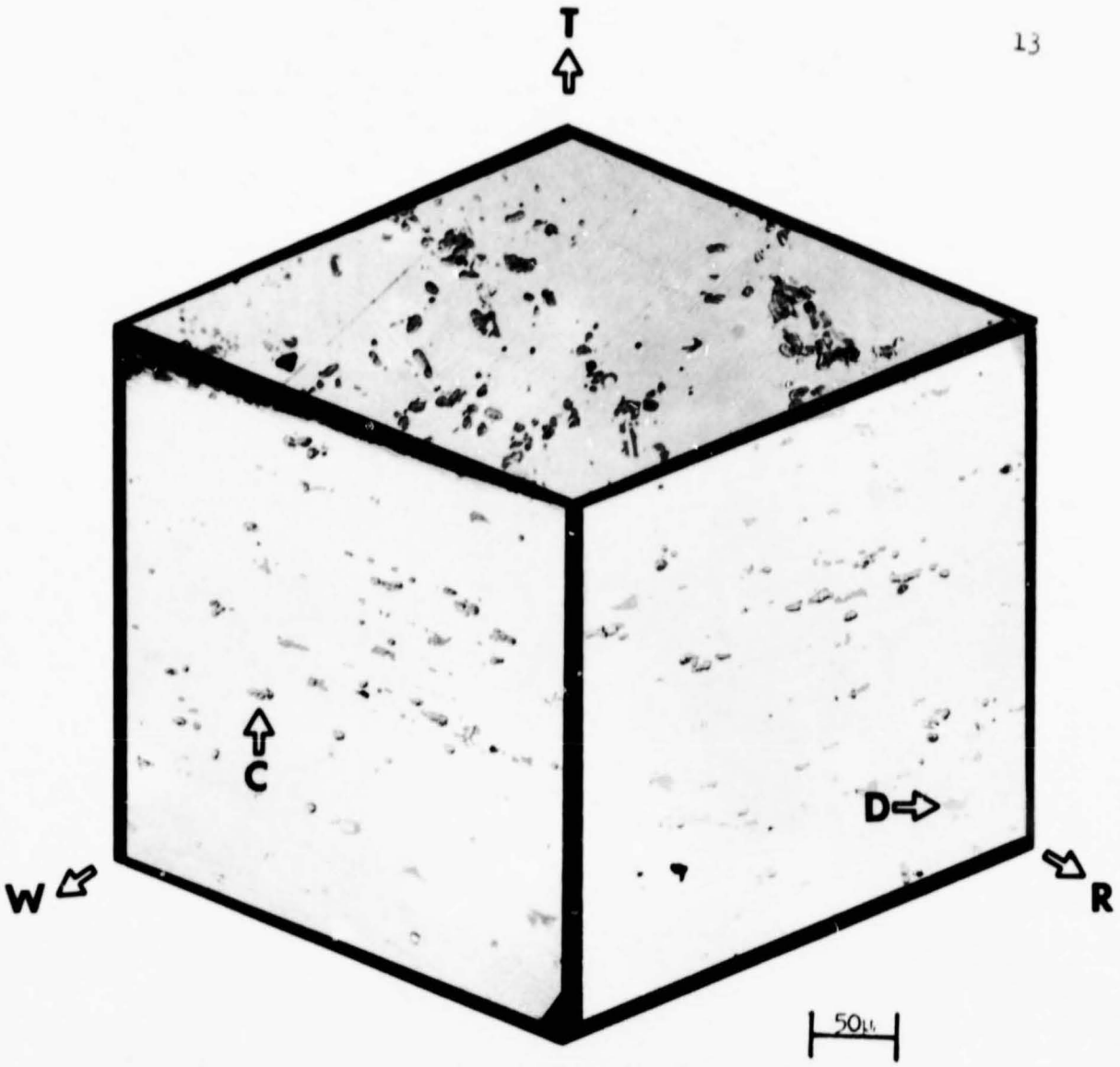

Figure 5 Micrographs of the Unetched Structure of 2014-T6 with Clear Gray (C) and Dark Gray (D) Particles. The Orientations Indicated are the Rolling (R), Transverse (W), and Thickness (T) Directions of the Plate.

Figure 6 Micrograph of the Midplane of a Strained Tensile Specimen of 2014-T6 with both Types of Particles Cracked. The Stress Axis is Horizontal.

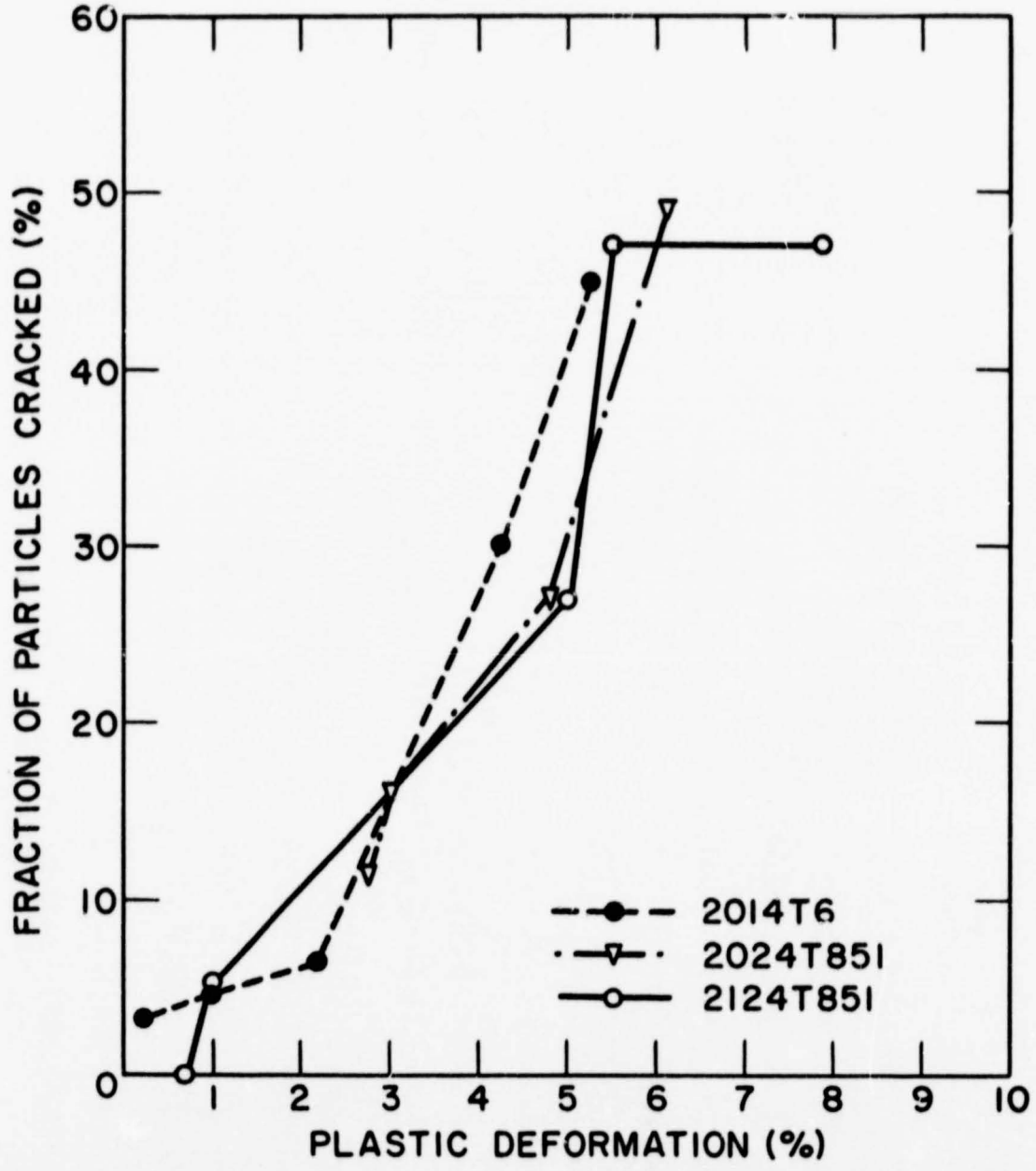

Figure 7 - Fraction of Second-Phase Particles Greater Than 2 Microns in Size which Cracked in Tensile Specimens Strained to Various Plastic Strains for 2014 T6, 2024 T851, and 2124 T851.

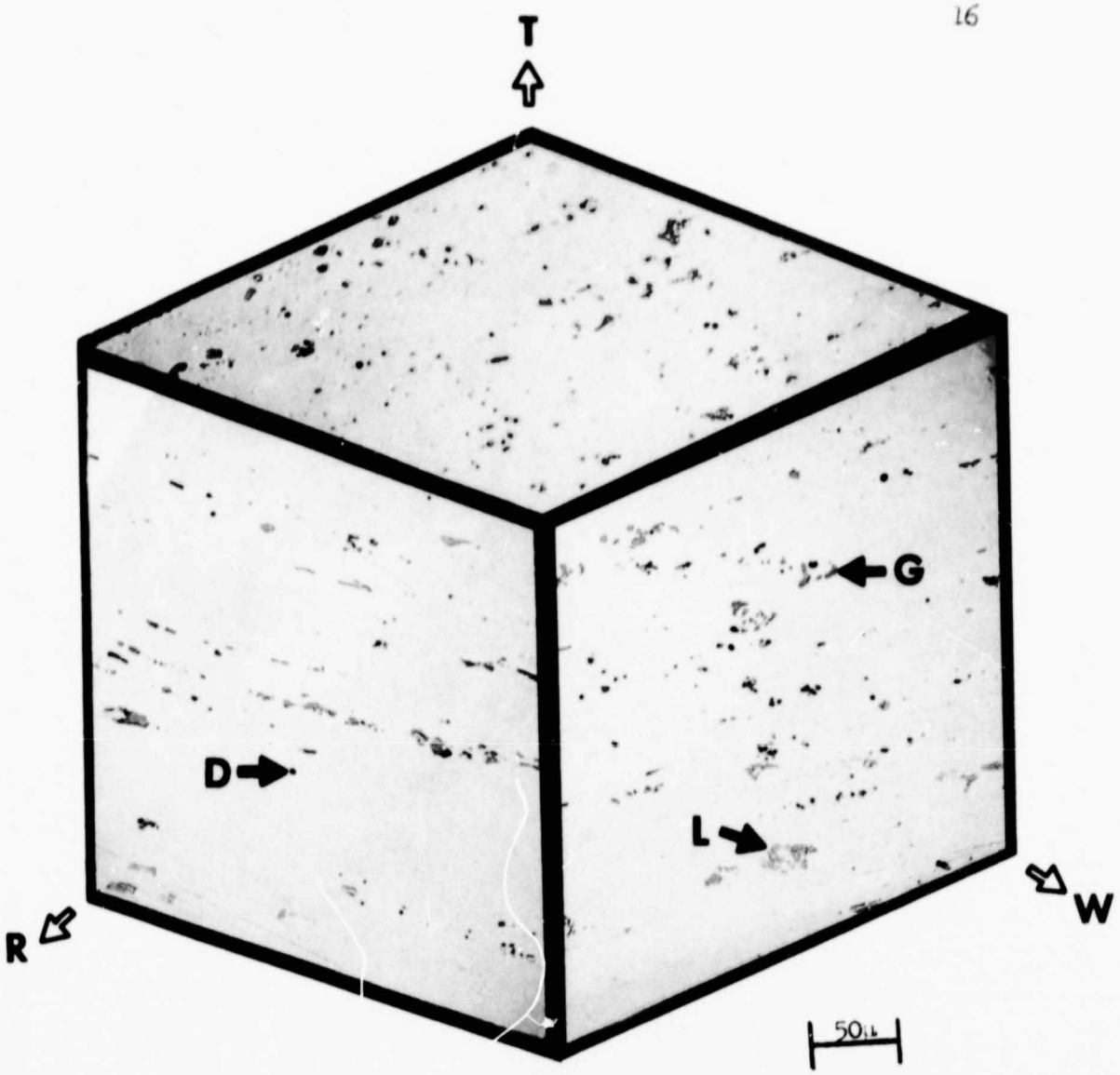

Figure 8 - Micrographs of the Unetched Structure of 2024 T851 with Light (L), Gray (G), and Dark (D) Second-Phase Particles. The Orientations Indicated are the Rolling (R), Transverse (W), and Thickness (T) Directions.

strains of less than 2.7% in the optical microscope, as shown in Figure 9. At higher strains, SEM studies showed that the dark particles (D) also cracked, as shown in Figure 10, with a specimen strained to 7.6% elongation. The particles which appear dark in the light microscope are darker than the aluminum matrix in the SEM. Figure 7 shows the cracking data for the light and gray particles combined.

C. 2124-T851

Due to the low impurity content in this alloy, there is only one type of second-phase particle, as shown in Figure 11. The cracking data for this alloy is also shown in Figure 7. It should be noted that at plastic strains of less than 0.7%, no particles have cracked. Because this alloy has only one type of second-phase particle, it will be used to show the effects of advanced stages of plastic deformation and its effects on the initiation of fracture. All the alloys were similar to 2124-T851 as far as the development of voids is concerned. Figure 12 shows a series of micrographs of polished midplanes of tensile specimens at various stages of deformation. In all cases, the axis of applied stress is the horizontal direction. Figure 12a shows a polished unstrained section while Figures 12b and 12c show sections strained 2.5% and regions near the fracture surface of specimens strained to rupture, respectively. The largest particles are cracked and some voids are starting to form in the 2.5% strained specimen. In the ruptured specimen, many more particles have cracked and

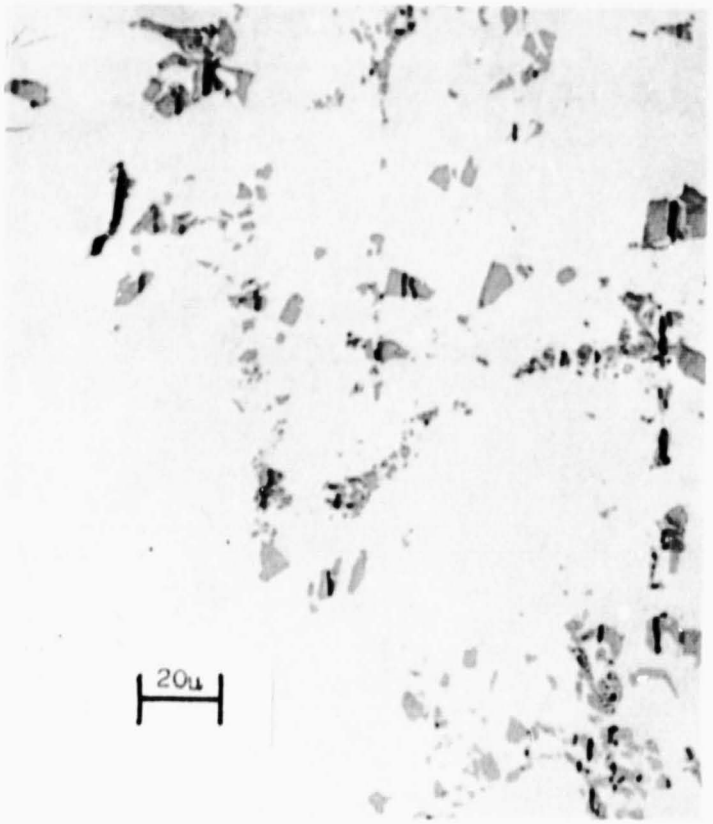

Figure 9 Micrograph of a Tensile Specimen of 2024-T851 Strained to 6.1%. Only the Light and Gray Particles are Observed to Crack. The Stress Axis is Horizontal.

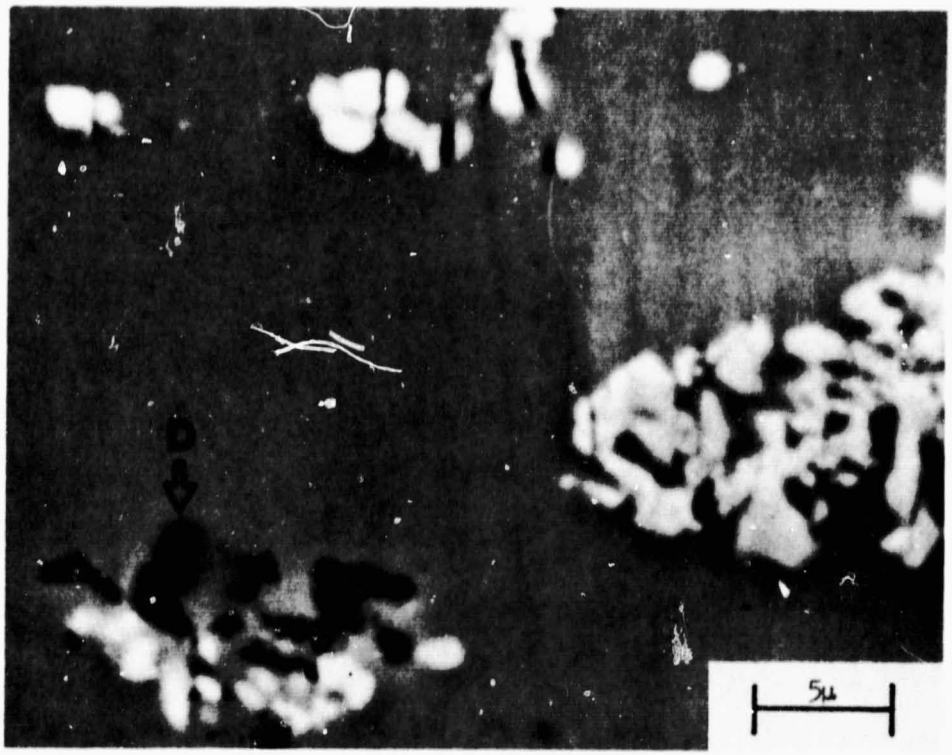

Figure 10 SEM Micrograph of a Tensile Specimen of 2024-T851 Strained to 7.6%. The Particle which Appears Darker than the Matrix (D) is a Dark Particle and is Observed to Crack at this Deformation. The Stress Axis is Horizontal.

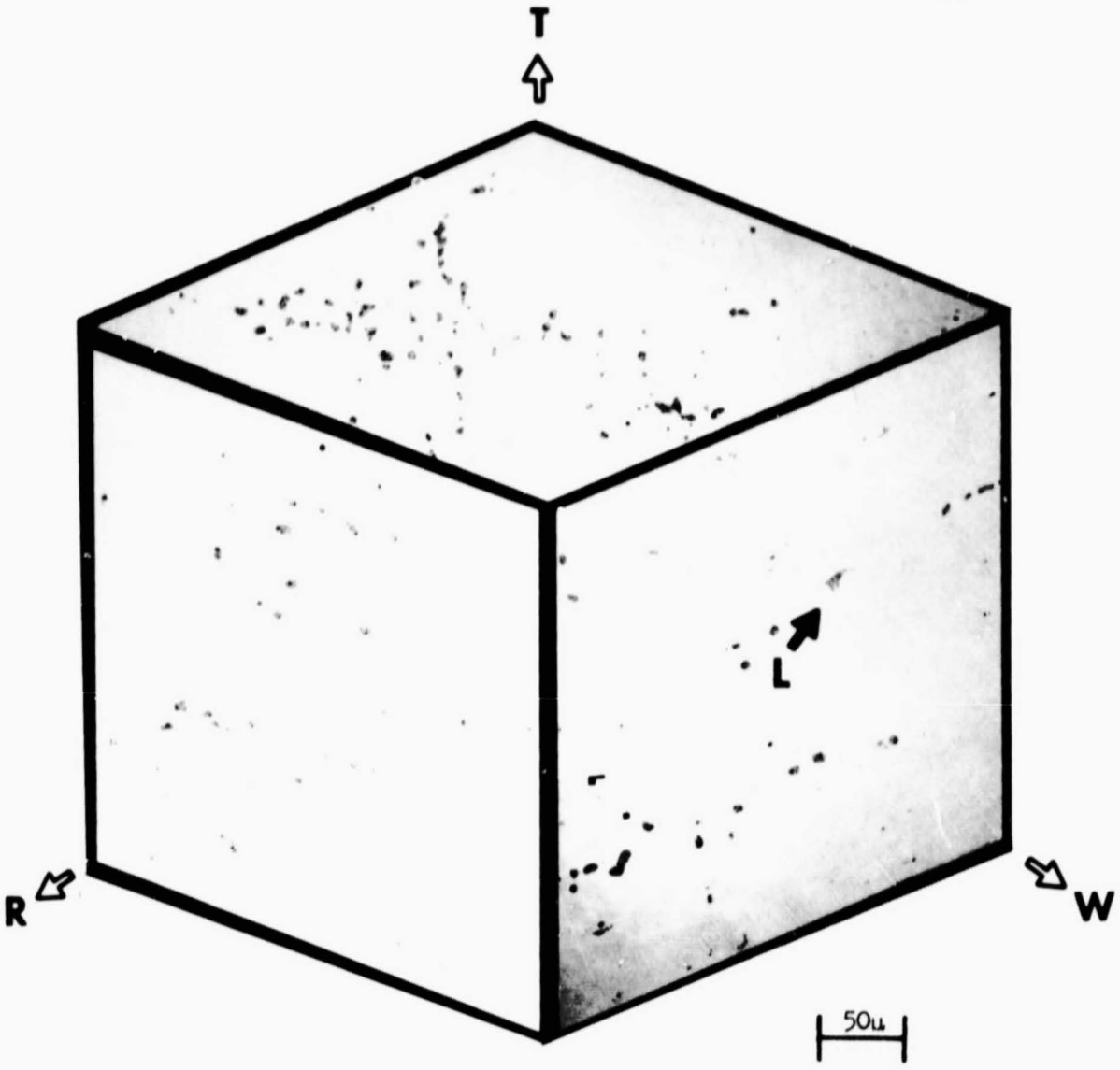

Figure 11 - Micrographs of the Unetched Structure of 2124 T851 with Light (L) Second-Phase Particles. The Orientations Indicated are the Rolling (R), Transverse (W), and Thickness (T) Directions.

Figure 12a

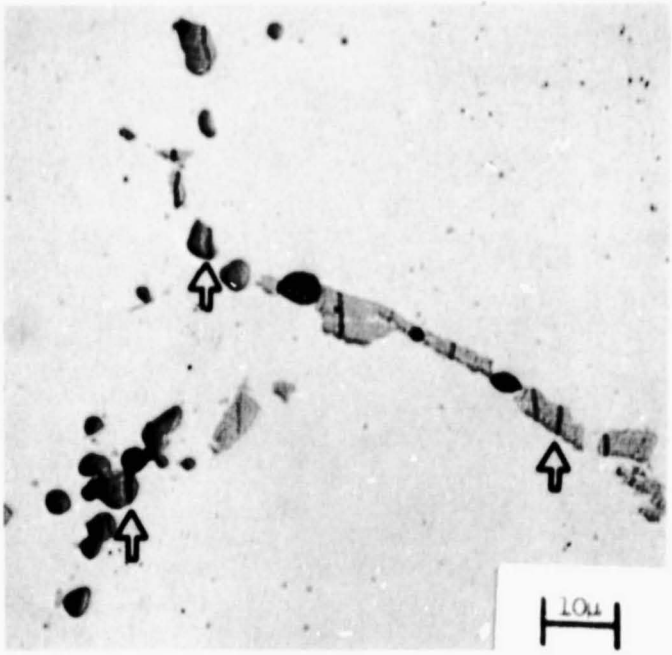

Figure 12b

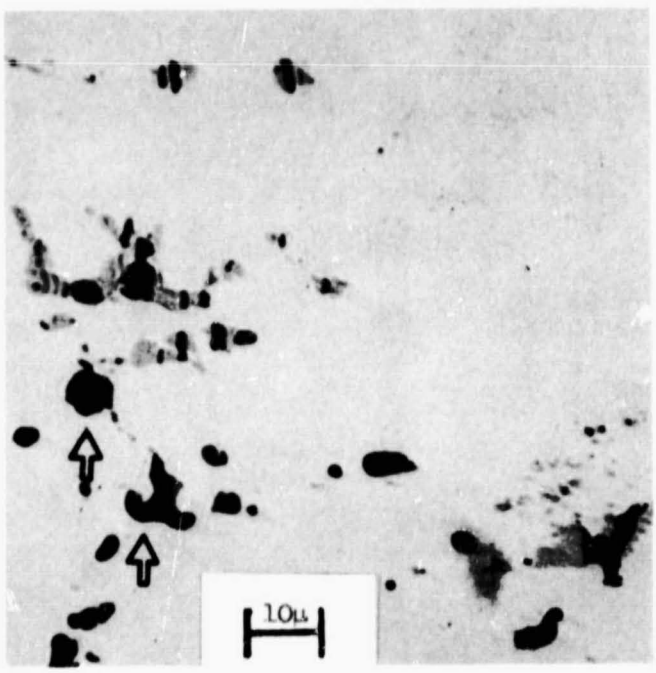

Figure 12c

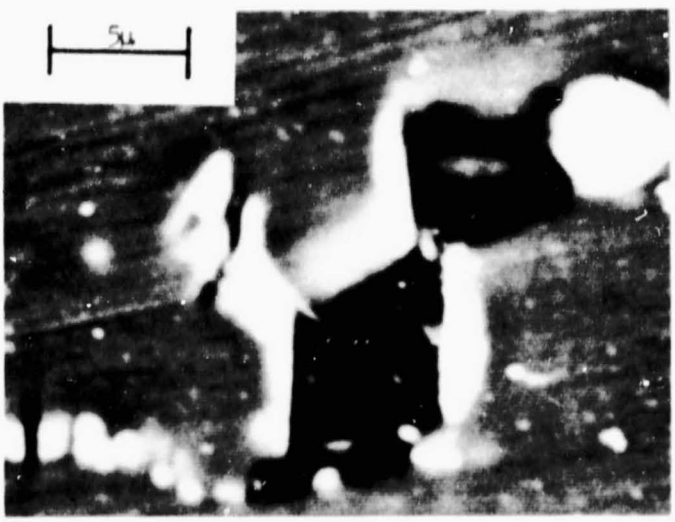

Figure 12d

Figure 12 Micrographs of a Tensile Specimen of 2124-T851 to Show the Effects of Plastic Deformation on the Void Initiation and Growth Stages of Plastic Fracture. The Stress Axis is Horizontal: (a) Shows an Unstrained Cross-Section, (b) Shows a Specimen with 2.5% Elongation with Cracked Particles, (c) Shows a Section Near the Fracture Surface of a Ruptured Tensile Specimen with Many Voids, (d) Shows an SEM Micrograph of a Second-Phase Particle and the Void Associated with it Near the Fracture Surface of a Ruptured Tensile Specimen.

voids 5 to 10 microns in size are associated with the largest particles which are approximately 5 microns in diameter. Figure 12d shows an SEM micrograph of voids formed in a specimen strained to rupture. Note that in micrographs of ruptured specimens (Figures 12c and 12d), the voids are as large as the nucleating particles; and they are also starting to grow out into the matrix in a direction perpendicular to the stress axis.

D. 7075-T7351

This alloy has two types of second-phase particles, a light (L) and dark (D) type, as shown in Figure 13. No cracked particles were observed until tensile specimen were strained more than 2.7%. At first, only the light particles cracked, as shown in the micrograph in Figure 14 of a specimen strained to 6%. Again, the large particles cracked first. In this alloy, large particles have cracked in several places. SEM investigation of a specimen strained 11.2% is shown in Figure 15 and indicates that at this strain the dark particles, which appear darker than the aluminum matrix, have also cracked. The cracking behavior of the light particles as a function of elongation is shown in Figure 16.

E. 7079-T651

Like 7075-T7351, this alloy has a light (L) and dark (D) second-phase particle, as shown in Figure 17. The light particles were not observed to crack until after more than 1.3% plastic deformation, as shown in Figure 16. The morphology of particle cracking is very similar to that of 7075-T7351, as shown in Figures 18 and

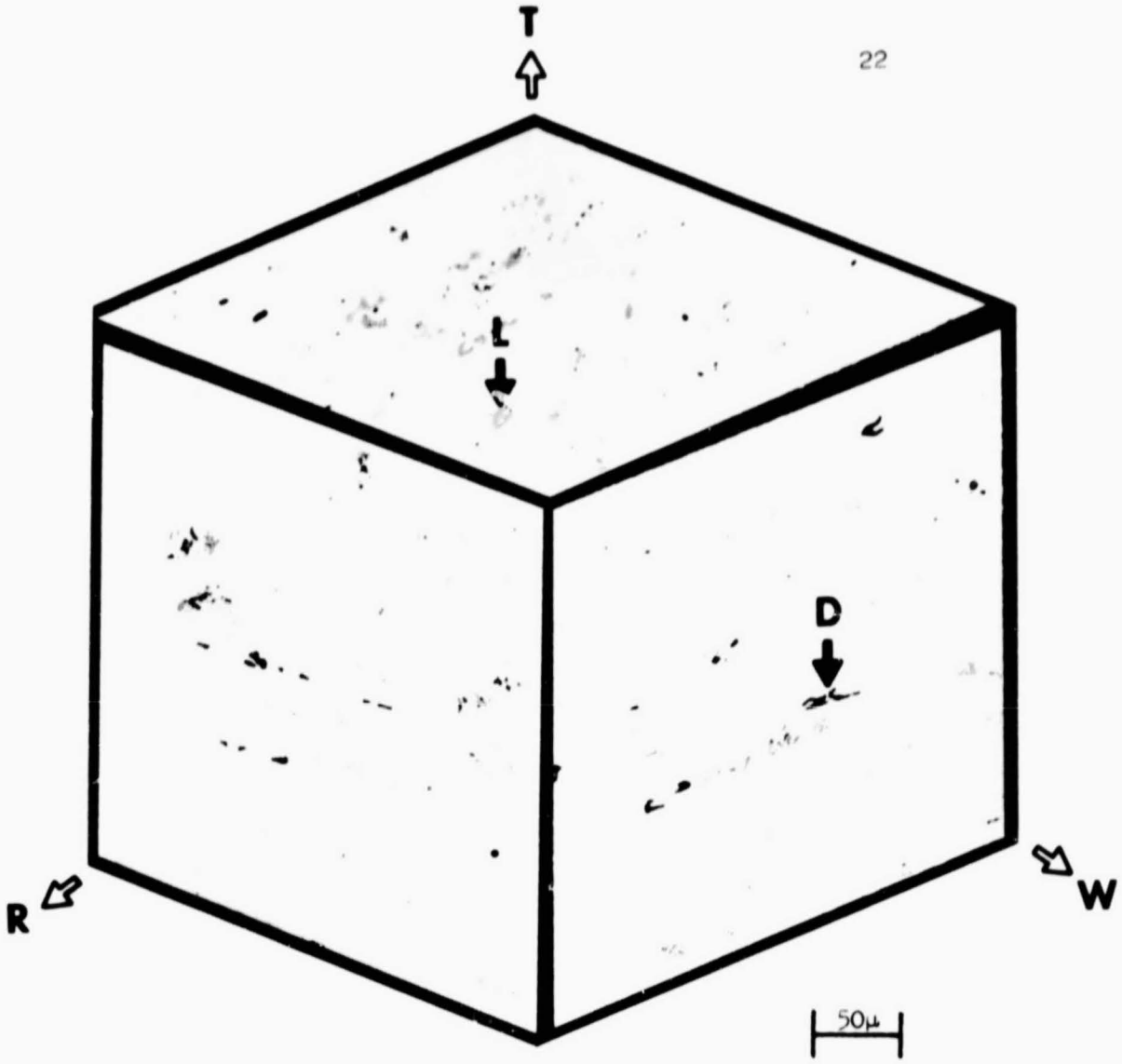

Figure 13 - Micrographs of the Unetched Structure of 7075 T7351 with Light (L) and Dark (D) Second-Phase Particles. The Orientations Indicated are the Rolling (R), Transverse (W), and Thickness (T) Directions.

Figure 14 Micrograph of a Tensile Specimen of 7075-T351 Strained to 6% with Cracked Light Particles. The Stress Axis is Horizontal.

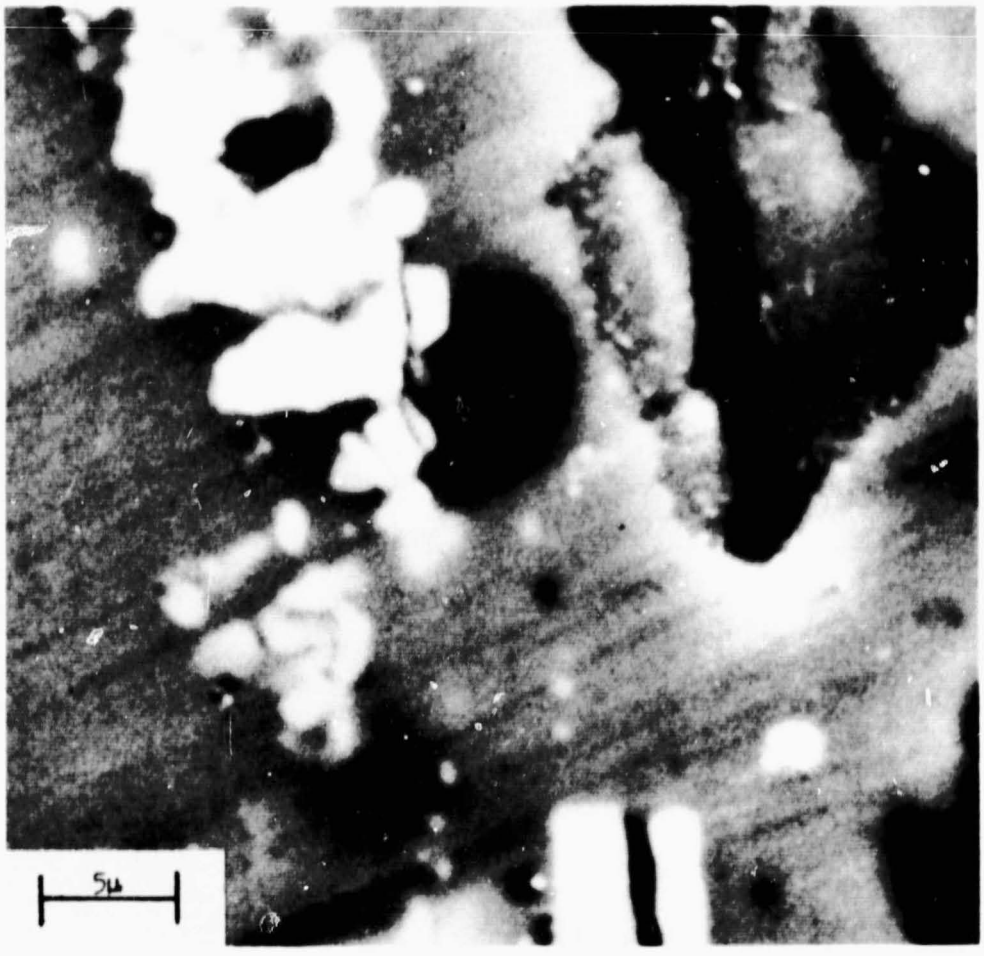

Figure 15 SEM Micrograph of a Tensile Specimen of 7075-T351 Strained to 11.2% with a Cracked Light and Dark Particles. The Stress Axis is Horizontal

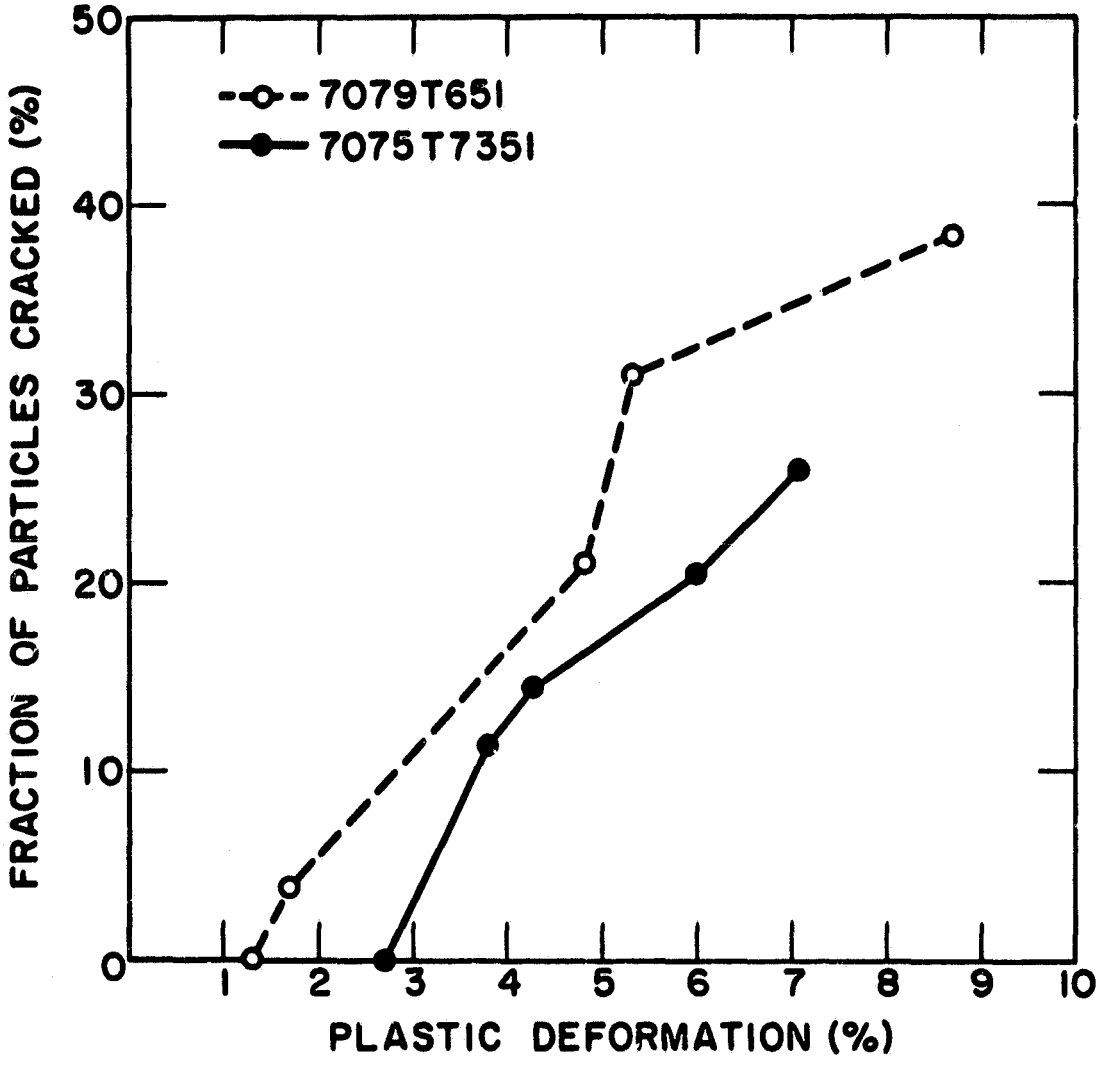

Figure 16 - Fraction of Second-Phase Particles Greater Than 2 Microns in Size which Cracked in Tensile Specimens Strained to Various Plastic Strains for 7075 T7351 and 7079 T651.

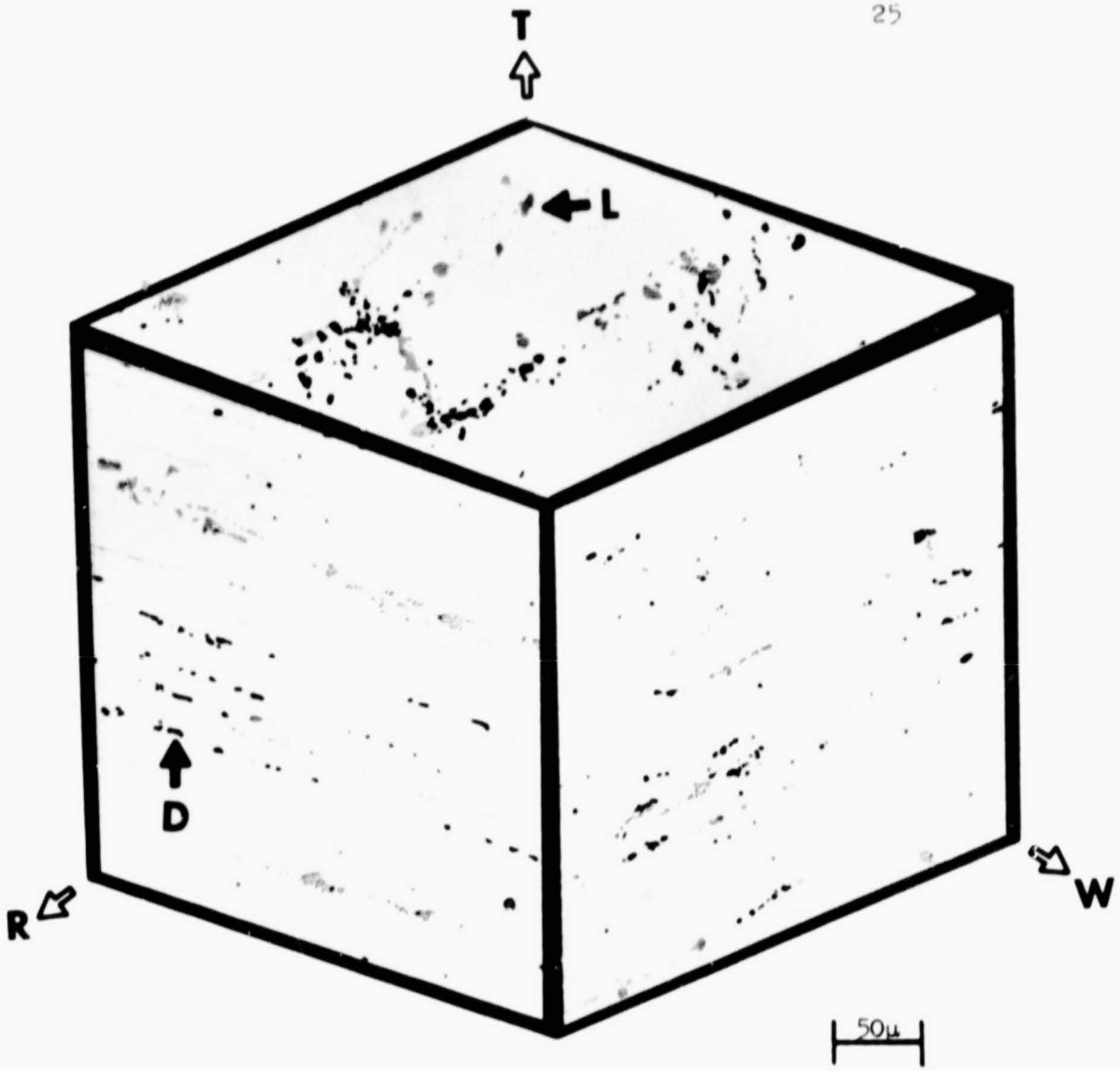

Figure 17 - Micrograph of the Unetched Structure of 7079 T651 with Light (L) and Dark (D) Second-Phase Particles. The Orientations Indicated are the Rolling (R), Transverse (W), and Thickness (T) Directions.

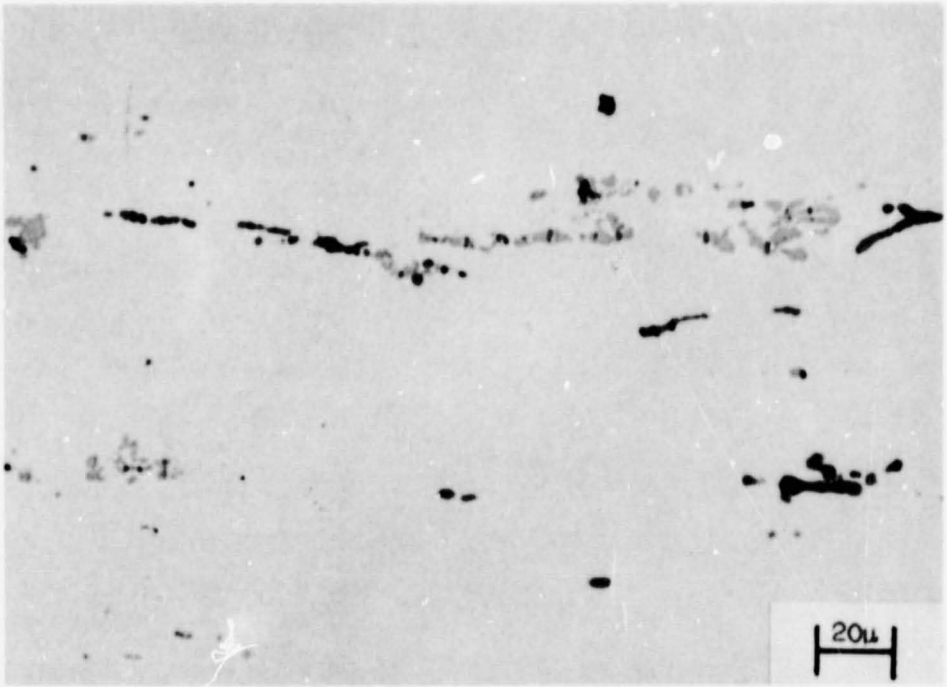

Figure 18 - Micrograph of a Tensile Specimen of 7079 T651 Strained to 4.8% with Cracked Light Particles. The Stress Axis is Horizontal.

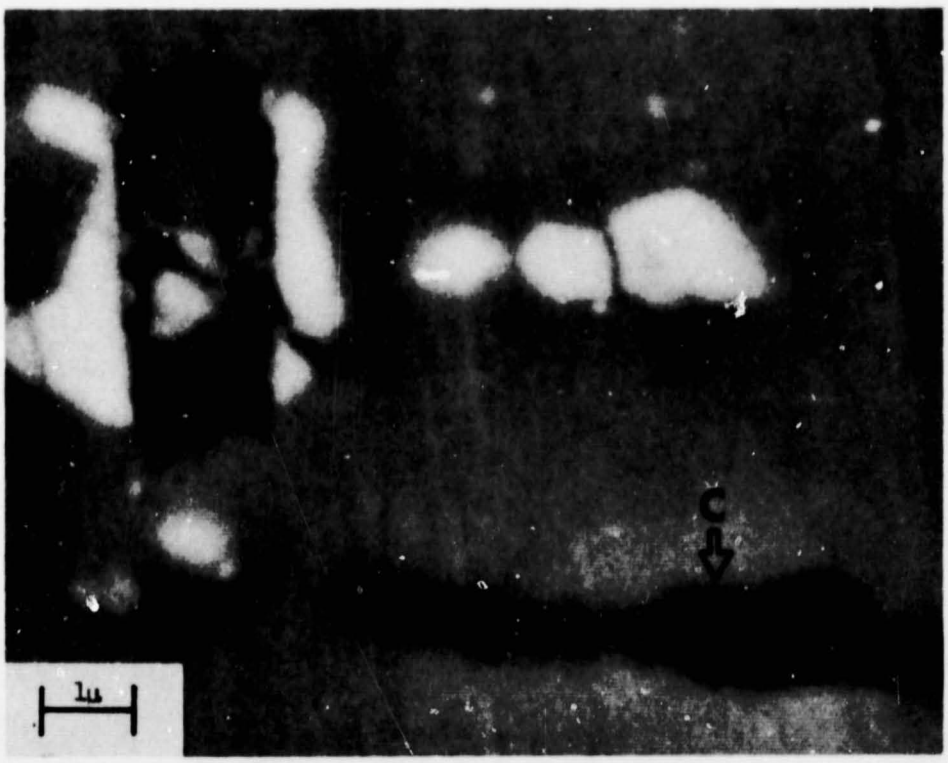

Figure 19 - SEM Micrograph of a Tensile Specimen of 7079 T651 Strained to 11.6% with a Large Void (V) at a Light Particle and a Cracked Dark Particle (C).

19. Figure 18 shows an optical micrograph of a specimen strained to 4.8%, and Figure 19 shows an SEM micrograph of a specimen strained to 11.6%. Again there are several cracks in the large particles. Figure 19 shows a large void formed by the light particle (V) and cracks (C) in the dark particle.

As these alloys are strained, the second phase particles crack to serve as initiation sites for voids. In the late stages of deformation, many voids are readily visible.

Indentification of Second Phase Particles

In order to suggest possible chemistry changes to decrease the particles which are the initiation sites for voids and thus improve the toughness, the chemical compositions of the second phase particles were determined.

A. 2014-T6

In the previous investigation[2] on 2014-T6, the authors determined that the composition of the dark gray particle was close to that of $Al_{12}(Fe,Mn)_3Si$ through extraction replicas. The light gray particles could not be extracted, but microprobe analysis from polished surfaces revealed the presence of aluminum, silicon, copper, and possibly magnesium, a phase commonly called the Q-Phase[6] which composition is close to $Al_4CuMgSi_4$[7]. It was not possible to determine if the lighter particle could not be extracted because it was not a void-nucleating particle or the extraction technique was not suitable for its extraction.

In either case, a decrease in iron and silicon would decrease the amount of the phases which are expected to be detrimental to fracture toughness.

In the other four alloys studied in this phase of the investigation, the elements in the second phase particles have been determined by inspection of polished surfaces by energy dispersion X-ray detector on a scanning electron microscope. The large penetration distance of electrons in aluminum with respect to the size of the second phase particles caused the results to reflect the composition of the matrix. Thus the results obtained are only qualitative in nature. Extraction replicas will be attempted in the next phase of the investigation.

B. 2024-T851

Analysis of the particles in 2024-T851 show that the dark particles contain magnesium and silicon while the light and gray ones contain aluminum, iron, manganese, and copper. H. Y. Hunsicker, W. A. Anderson, and W. G. Fricke [6] have suggested that the light and gray phases are $Al_2Cu(Mn,Fe)_3$ and $CuAl_2$ and the dark phase is Mg_2Si. Some recent work by Vruggink and Fricke [6] have compared microprobe trace analysis of polished surfaces and fracture surfaces pressed flat into a tungsten carbide block. Their results for 2024-T851 show that the fracture surface had higher manganese, iron, and copper concentration than polished surfaces, indicating that the void-nucleating particles contained substantial amounts of those elements. The cracking study on 2024-T851 indicated that the light and gray particles are the

void-nucleating particles. The qualitative analyses of these particles given above agree with the results of Vruggink and Fricke [6].

C. 2124-T851

In 2124-T851, the SEM investigation has shown that the second phase particles contain copper, manganese, and aluminum. Hunsicker, et. al. [6] have identified this phase as $Al_{20}Cu_2(Mn,Fe)_3$. The silicon content of this alloy is close to the solid solubility of silicon in aluminum [7] so no phase containing silicon was observed.

D. 7075-T7351

Analyses of the observed particles in 7075-T7351 showed the dark ones contained magnesium and silicon while the light particles contained copper, iron, and manganese. In a recent review article, Mondolfo [8] has indicated at the Fe/Mn ratio the nonequilibrium $FeAl_6$ will form. Manganese can replace up to 7% of the iron in $FeAl_6$ and tends to stabilize it as does copper. Mondolfo also indicates that Mg_2Si will form. Hunsicker, et. al. [6] give the same conclusions.

E. 7079-T651

SEM investigation of 7079-T651 shows that the particles in this alloy contain the same elements as 7075-T7351. Mondolfo [8] indicates that at the Fe/Mn ratio of 7079-T651, $MnAl_6$ will form but up to 19% iron and up to 2% copper can replace manganese and some aluminum. He also indicates that Mg_2Si will be present. This was verified by Hunsicker, et. al. [6].

The qualitative analyses and presumed compounds are summarized in Table IV.

Quantitative Metallography of Large Second Phase Particles

In order to correlate the fracture characteristics of the void-nucleating particles with fractographic evidence and K_{I_c} fracture toughness values, these particles must be characterized quantitatively to describe their morphology and distribution. From the micrographs of these alloys shown previously (Figures 5, 8, 11, 13, and 17), it is obvious that the apparent shape of the particles varies with the orientation of the plane of sectioning. The shape of the particles is very complex, probably due to interdendritic solidification and deformation during hot rolling. For this reason, quantitative measurements were made to characterize particles with two axes of preferred orientation as a cross-rolled product would have. The method of DeHoff [9] was used where each particle is assumed to have the same ellipsoidal shape. The average dimension in the rolling, transverse, and thickness directions (d_R,d_W,d_T), and number of particles per unit volume (N_v) were determined. From this information, the volume fraction (v/o) was calculated and the three-dimensional center-to-center spacing (λ) was determined from the following equation [10]:

$$\lambda = 0.554\ (N_v)^{-1/3} \qquad \text{Eq.(2)}$$

The data were obtained using a Bausch and Lomb Quantitative Metallurgical System at the Alcoa Technical Center through the courtesy of W. G. Fricke and R. H. Stevens. So that this data could be compared

TABLE IV

Composition of Second-Phase Particles

Alloy	Particle Description	Elements in Particle	Presumed Phase Composition
2014-T6	Clear Gray	Al, Si, Cu, Mg	Q-Phase ($Al_4CuMgSi_4$)
	Dark Gray	-	$Al_{12}(Fe, Mn)_3Si$
2024-T851	Light	Al, Fe	$Al_2Cu(Mn,Fe)_3$
	Gray	Mn, Cu	$CuAl_2$
	Dark	Mg, Si	Mg_2Si
2124-T851	Light	Al, Cu, Mn	$Al_{20}Cu_2(Mn, Fe)_3$
7075-T7351	Light	Fe, Cu, Mn	$(Fe, Mn, Cu)Al_6$
	Dark	Mg, Si	Mg_2Si
7079-T651	Light	Fe, Cu, Mn	$(Mn, Fe, Cu)Al_6$
	Dark	Mg, Si	Mg_2Si

with the particle cracking data, no particle smaller than 2 microns was counted. The results are shown in Table V. Also shown are combined populations identified as void initiating populations. These are the data from two types of particles if two types of particles were observed to crack. The data for the dark particles in 2024-T851 and 7075-T7351 are questionable due to the small number of particles observed. Data for the light particles in 2024-T851 could not be determined due to the small number, but the combined population of the gray and light particles was determined.

Due to the clustering of these particles which can be observed in the micrographs, the standard deviation on the data is quite large. It is felt that this reflects the clustering effect and not the manner in which the data were taken.

Transmission Electron Microscopy

The strength of these alloys comes primarily from dislocations being pinned by precipitates formed during the aging treatment and small intermetallic dispersoid particles formed during solidification. These were both observed in the previous investigation[2], and it was suggested that the intermetallic dispersoid particles may serve as the nucleation sites for the small dimples observed in the fractographs. For this reason, quantitative transmission electron microscopy was used to describe the small intermetallic dispersoids. The method of Cahn and Nutting [11] which is based on spheres and gives average number per volume and average dispersoid diameter was used. To utilize this method the thickness of the foil

TABLE V

Quantitative Metallography on Second-Phase Particles

(* Indicates Void Nucleating Particles)

Alloy	Particle Description	Number Per Volume ($10^7/cm^3$)	Volume Fraction (%)	Center-to-Center Spacing (μ)	d_R (Rolling) (μ)	d_W (Transverse) (μ)	d_T (Thickness) (μ)
2014-T6	Clear Gray	21.9	1.5	9.2	6.5	4.4	4.6
	Dark Gray	7.3	1.5	13.3	9.7	9.3	4.7
	Clear & Dark Gray*	29.2	2.9	8.4	7.2	5.6	4.6
2024-T851	Gray	17.0	0.2	10.0	2.2	0.8	10.6
	Dark	0.7	1.7 (?)	28.8	36.6 (?)	13.8 (?)	8.9 (?)
	Light & Gray*	41.6	2.7	7.4	8.8	3.6	3.9
2124-T851	Light*	21.8	1.0	9.2	4.0	4.1	5.4
7075-T7351	Light*	9.3	0.4	12.2	5.0	3.1	4.8
	Dark	1.4	2.2 (?)	23.0	22.4 (?)	11.7 (?)	11.4 (?)
7079-T651	Light*	16.0	0.4	10.2	4.5	2.8	3.5
	Dark	4.7	0.5	15.3	6.2	4.7	6.4

in the region of observation must be determined. This was accomplished by observing the number of extinction contours at a grain boundary such as that shown in Figure 20. By solving the appropriate diffraction pattern, the extinction distance for that reflection could be found from standard tables, and the local foil thickness was then determined.

Micrographs for the five alloys are shown in Figures 21a through 21e. Note that in all the cases the dispersoids have diameters on the order of 0.1 micron.

In the 2000 series alloys, the dispersoids were sometimes cylindrically shaped but the approximation of spherical particles was made. They have been identified as $Al_{12}(Mn, Fe)_3Si$[6]. In the background of the 2000 series micrographs, the classic aluminum-copper acicular precipitates are shown. These are believed to be θ' precipitates which have been identified as $CuAl_2$[7]. They are shown at a higher magnification for 2124-T851 in Figure 22.

The 7000 series dipersoids are round and very close to being spheres. In the background of those micrographs in Figure 21d, the very diffuse elipsoidal precipitate structure can be observed. The chief precipitate in the Al-Mg-Zn system is the η phase which has been identified as $MgZn_2$[12]. The dispersoids in these two alloys appeared to be similar in size and shape to those observed in 7075-T7351 by Hunter and McMillan[13]. They identified the dispersoid as the E-Phase or $Al_{12}Mg_2Cr$. Hunsicker, et.al.[6] verified this result.

Table VI shows the results of the quantitative transmission

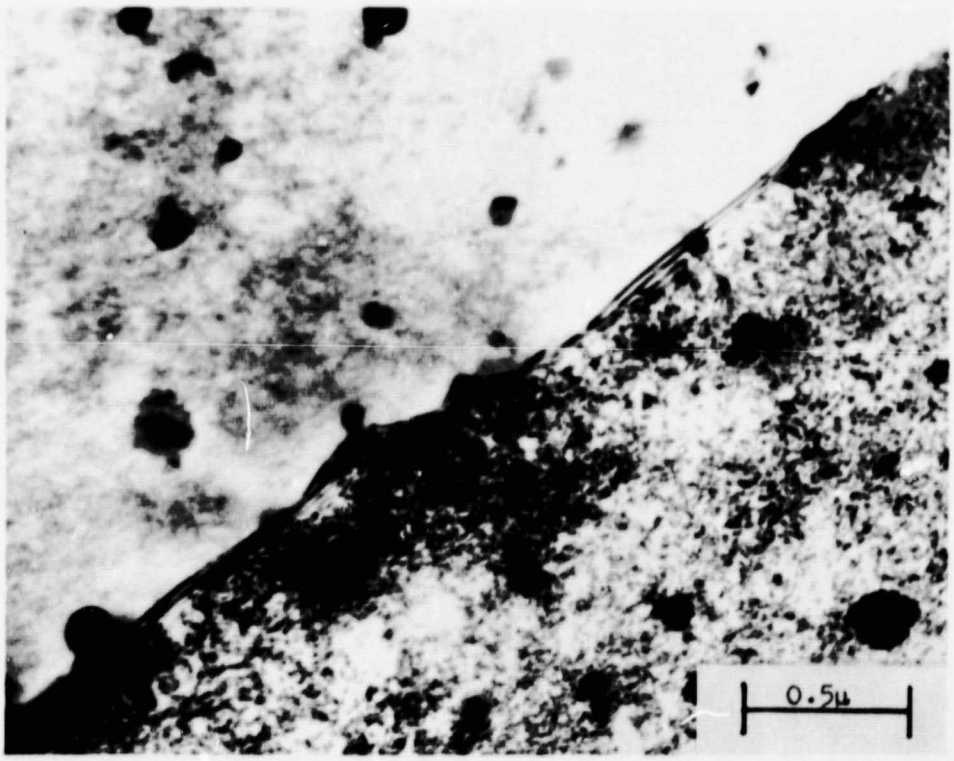

Figure 20 Transmission Electron Micrograph of an Extinction Contour on a Grain Boundary in 2014-T6.

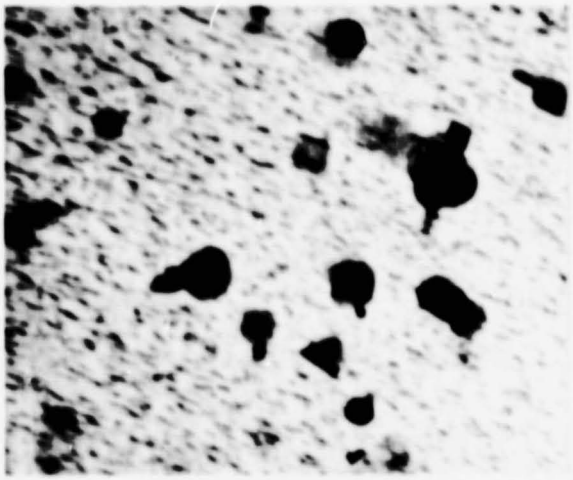

Figure 21a: 2014 T6

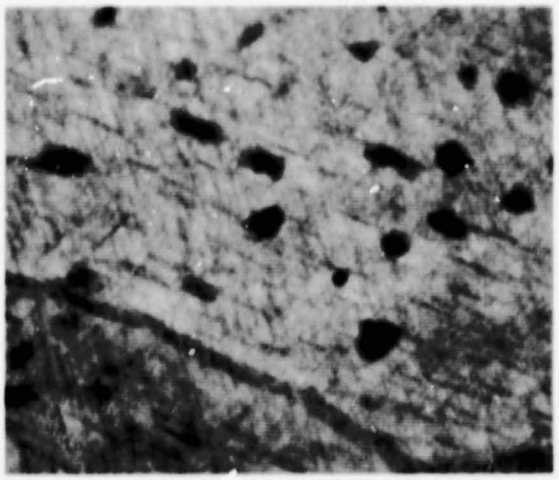

Figure 21b: 2024 T851

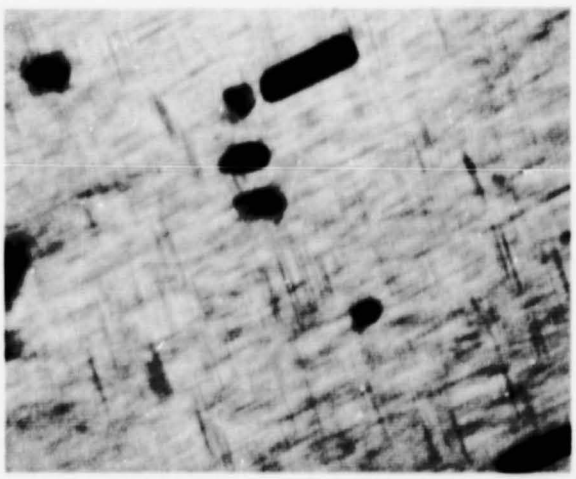

Figure 21c: 2124 T851

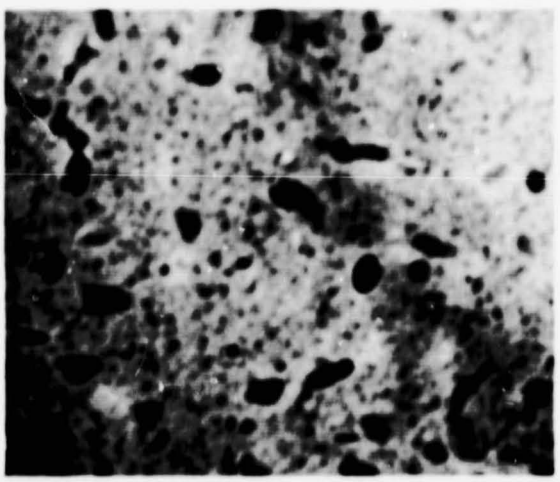

Figure 21d: 7075 T7351

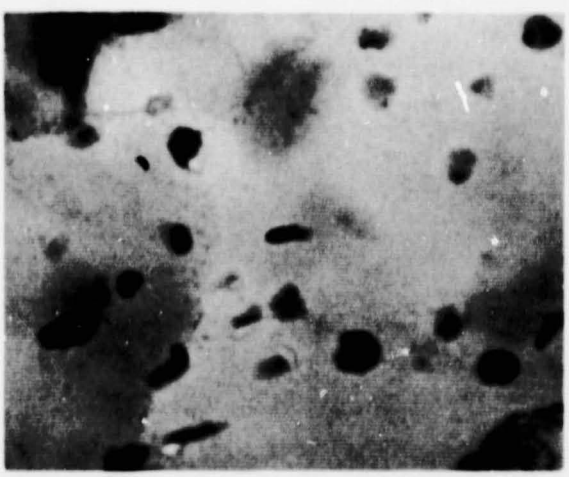

Figure 21e: 7079 T651

0.2μ

Figure 21 Dispersoid Structure of the Alloys:
(a) 2014-T6
(b) 2024-T851
(c) 2124-T851
(d) 7075-T7351
(e) 7079-T651

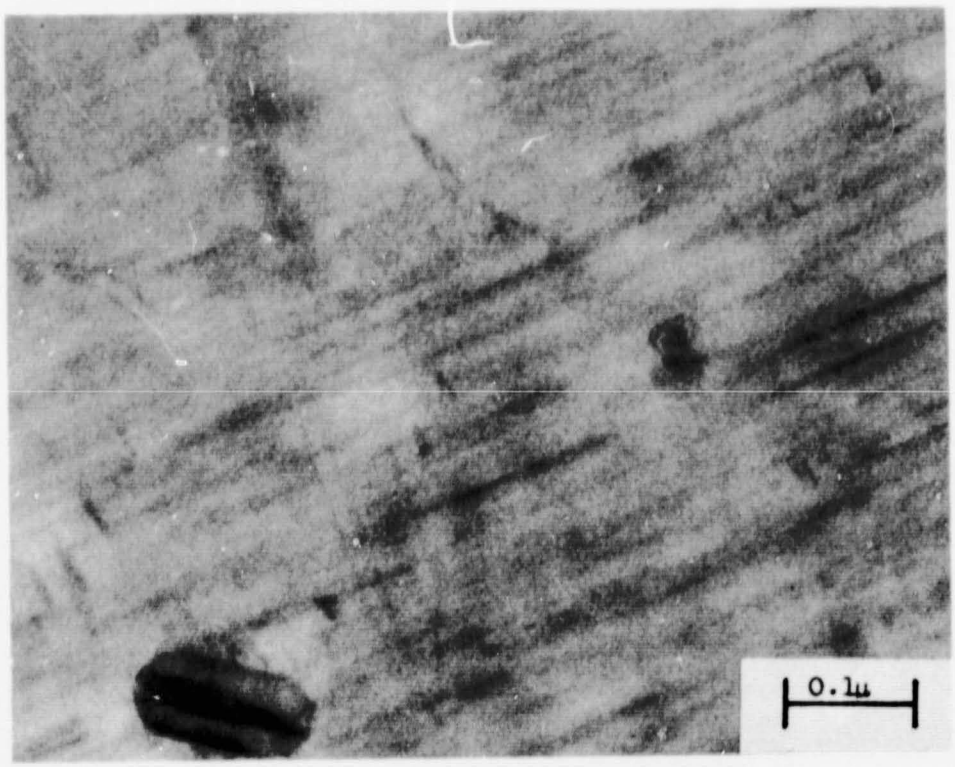

Figure 22 - Precipitate Structure of 2124 T851

TABLE VI

Dispersoid Data

Alloy	Dispersoid Diameter (Å)	Number Per Unit Volume ($10^{12}/cm^3$)	Center-to-Center Spacing (μ)
2014-T6	930	2.0	0.44
2024-T851	680	10.9	0.25
2124-T851	1010	4.7	0.33
7075-T7351	490	4.9	0.33
7079-T651	760	19.0	0.21

electron microscopy. Also shown in the table is the center-to-center spacing of the dispersoids as calculated by equation (2).

Correlation Between Microstructure and Fracture Characteristics

From the experimental evidence just described, it is possible to qualitatively describe the fracture processes in aluminum alloys. First, voids are initiated by the cracking of specific large second phase particles. As the load is increased the voids grow until a critical ligament size between voids is reached. At that point the final rupture occurs by formation of small voids which nucleate at the dispersoids in the ligaments between large voids. In order to suggest possible chemistry changes, the effect of microstructure on void initiation, growth, and coalescence must be assessed. At this point in the investigation, only empirical correlations are available.

A. Void Initiation

Naturally, as the composition of the particles change, the effect of stress will vary. In order to compare the cracking data shown in Figures 7 and 16 with fracture toughness, it must be presented as a function of stress so that it can be related to K_{I_c}, a stress instability criterion. One way to do this is to plot the fraction of cracked particles against the increment of stress in excess of the yield stress as shown in Figure 23. Comparison of that graph with the K_{I_c} fracture toughnesses listed in the figure shows that the cracking curves shift to the right as the toughness increases. As expected, a resistance

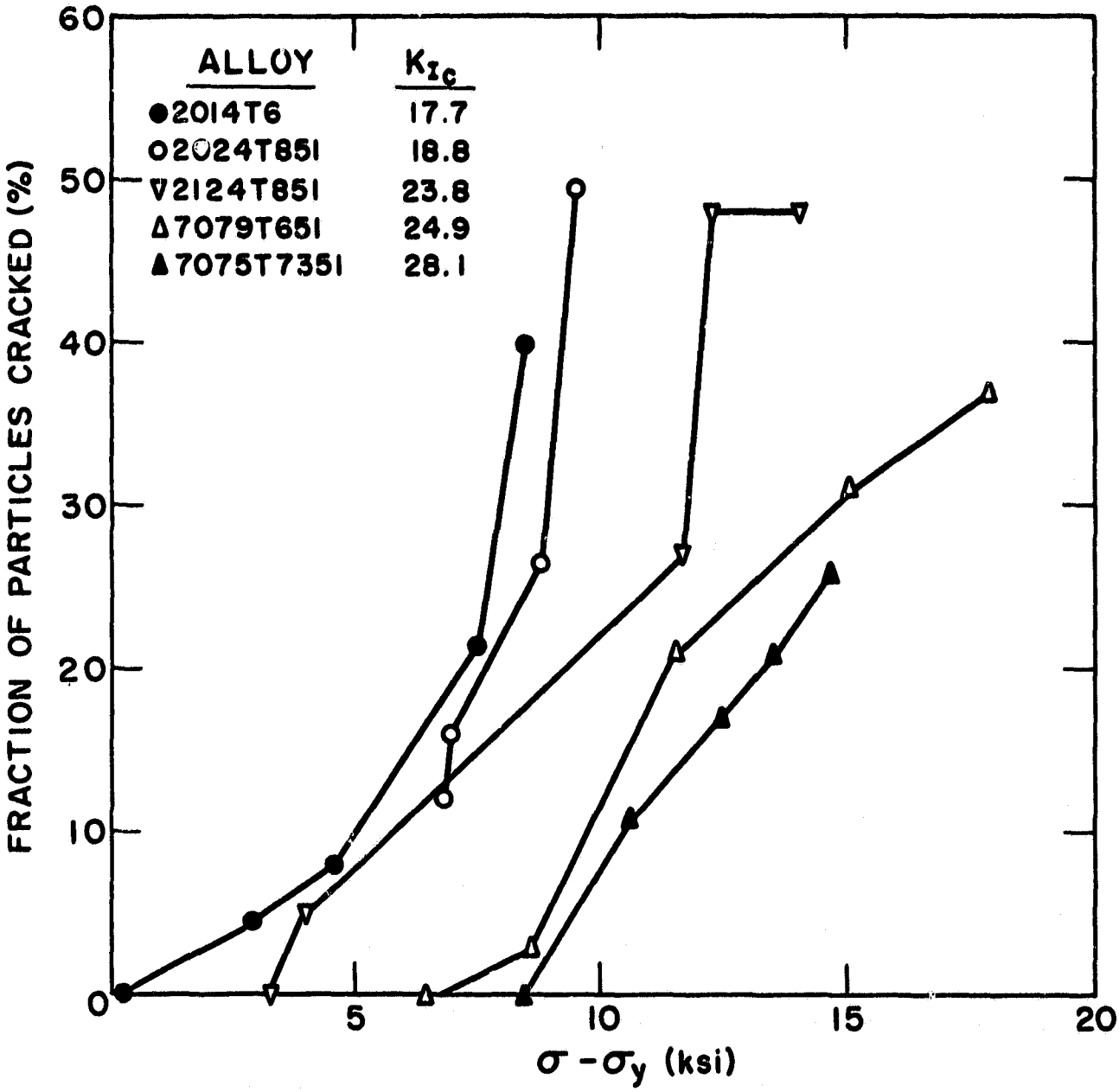

Figure 23 - Fraction of Second-Phase Particles Greater Than 2 Microns in Size which Cracked in Tensile Specimens as a Function of the Stress Increment Above the Yield Stress

to void initiation increases the toughness. The particle size effect which was noted qualitatively in the cracking study can be analyzed quantitatively by defining an equivalent particle diameter $\bar{d}$, measured in the plane normal to the tensile axis as:

$$\bar{d} = \sqrt{d_1 d_2} \qquad \text{Eq.(3)}$$

where d_1 and d_2 are the particle dimensions in that plane. Figure 24 shows the empirical relationship between $\bar{d}$ and the initiation of particle cracking. As the particle size decreases, the void initiation stage is retarded and toughness will increase. Gurland[14] and Ashby[15] have proposed models of void initiation which predict this effect.

B. Void Growth

Void growth is the most difficult stage of plastic fracture to analyze. In these alloys, the amount of void growth as measured by the void growth parameter as defined in equation (1) did not vary greatly (3.24 to 4.56). It is possible however that these small differences significantly affected the fracture toughness as shown in Figure 25. Very small changes in void growth behavior result in large increases in K_{I_c} fracture toughness. The process of void growth can be viewed as one which will continue to occur until two adjacent voids impinge or until interrupted by the coalescence stage. Coalescence probably occurs very quickly in the last stage of fracture, because no evidence of the joining up of the large voids was observed during

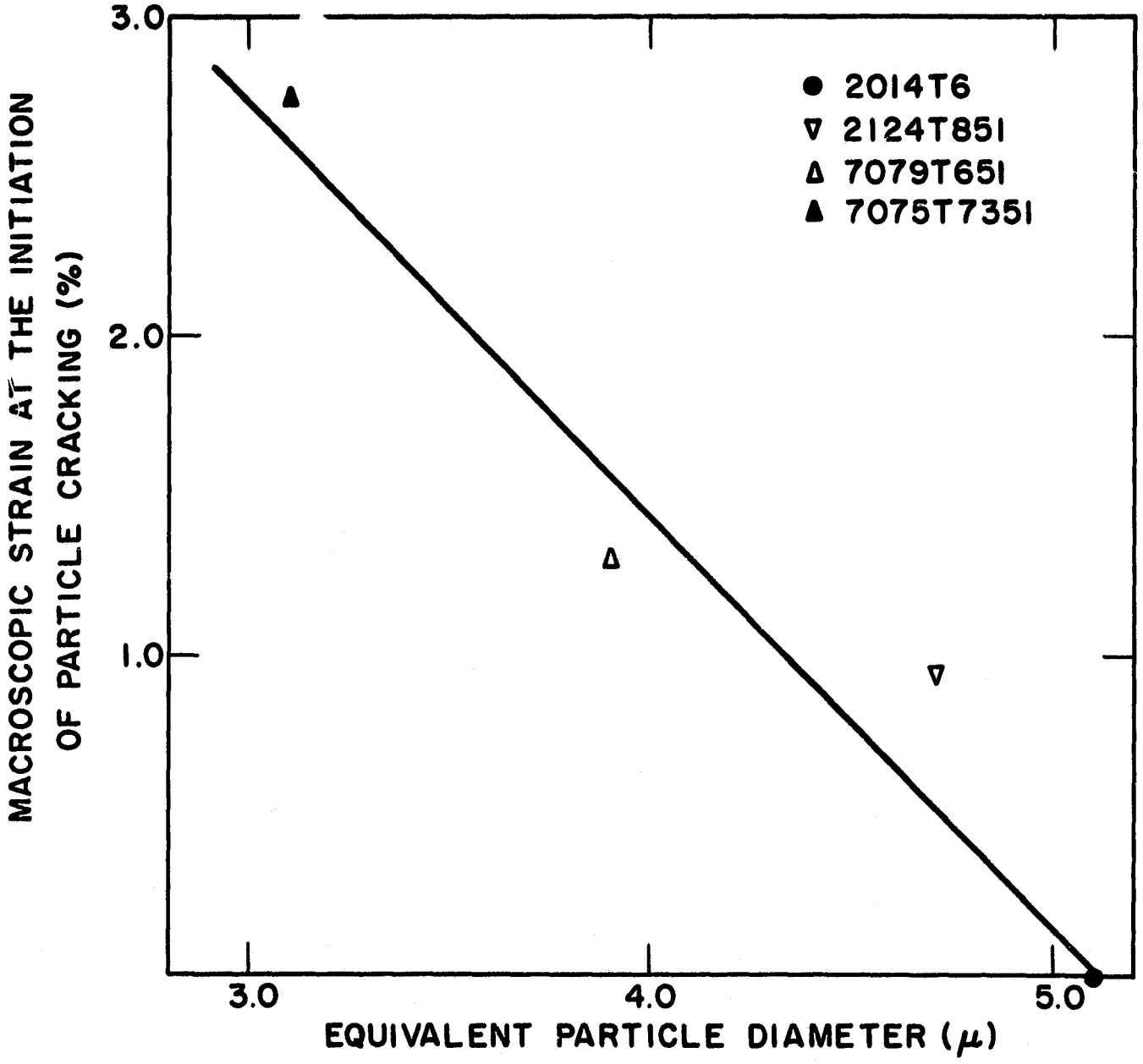

Figure 24 The Plastic Strain Necessary to Start Particle Cracking as a Function of the Effective Particle Diameter

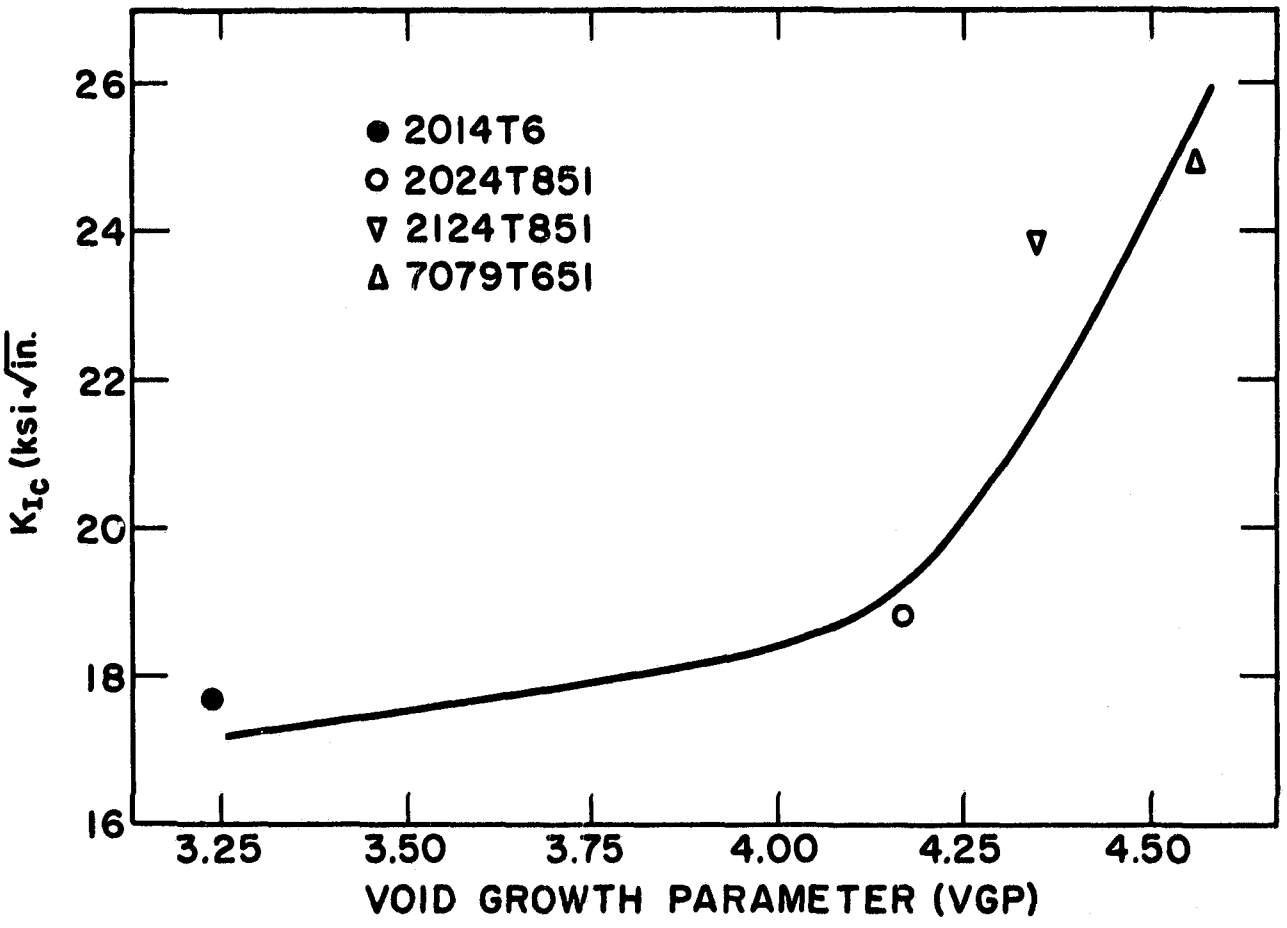

Figure 25 K_{Ic} Fracture Toughness as a Function of the Void Growth Parameter

the microscopic observations of tensile specimens, even in specimens strained almost to fracture. Thus, the concept of a critical ligament size between adjacent voids as the criteria for coalescence is not unreasonable. If this is the case, the void growth parameter should only be limited by spacing between the void nucleating second phase particles. Figure 26 shows that the void growth parameter increases as the particle spacing, indicating the voids will grow until the large dimples impinge on one another. Void growth is not affected until the spacing is greater than about 8 microns. Void growth can appreciably increase fracture toughness and is principally controlled by the spacing between void nucleating particles which is related to the number of particles through equation (2).

C. Void Coalescence

In the previous progress report[2], it was suggested that the 0.1 micron diameter dispersoids may serve as void nucleating particles in the coalescence stage of fracture. Palmer, Smith, and Warda[16] have observed particles as small as 50 Å nucleating voids in high purity internally oxidized copper. Broek[17] observed voids forming around dispersoids with diameters of about 5000 Å in thin foils of strained aluminum alloys including 2024. Figure 27 shows a plot of the dispersoid spacing (Table VI) against the small dimple spacing (Table III). The linear relationship indicates that the dispersoids served as nucleating sites for the small dimples. The slope of the plot is greater than

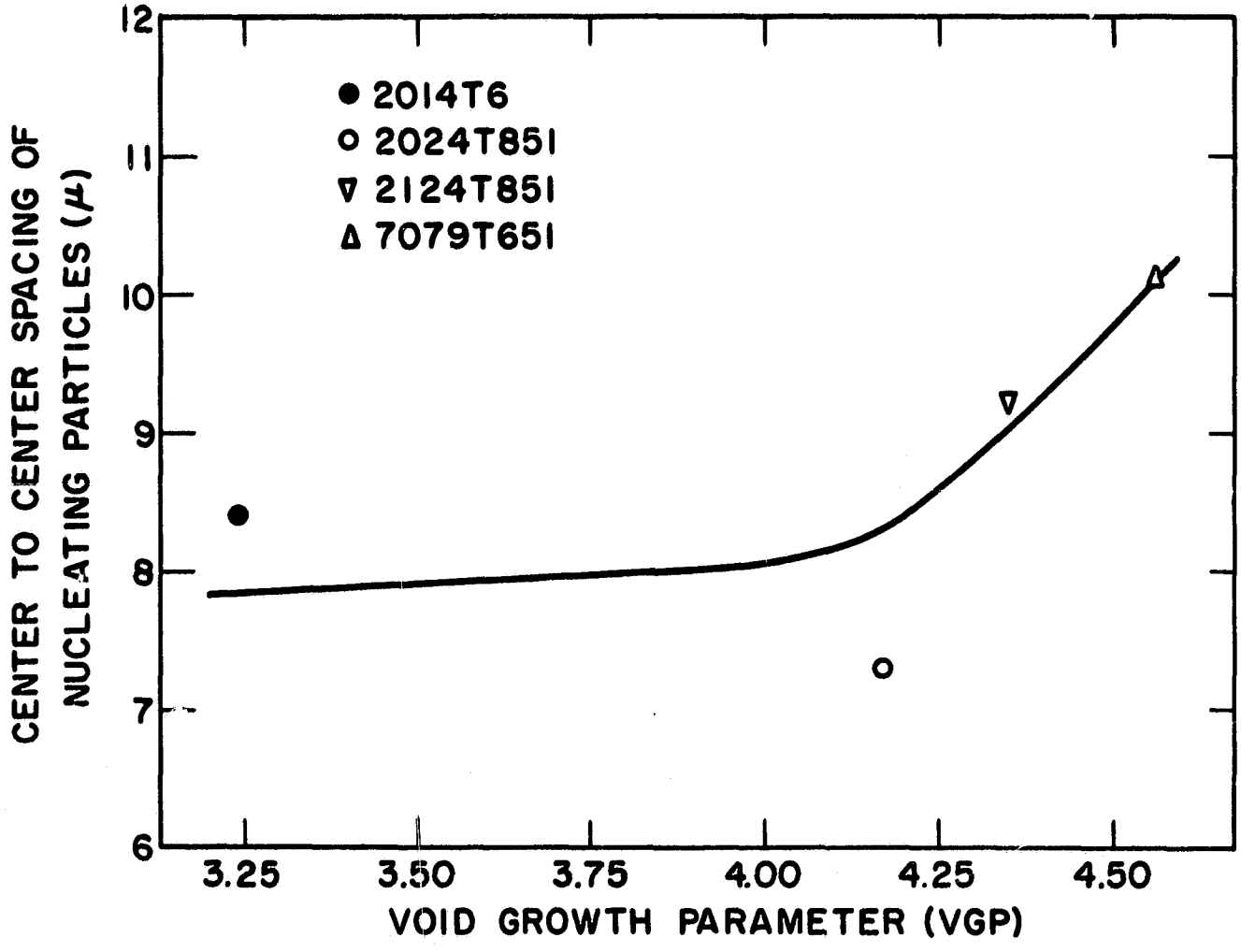

Figure 26 The Void Growth Parameter as a Function of the Center-To-Center Spacing of the Void-Nucleating Particles

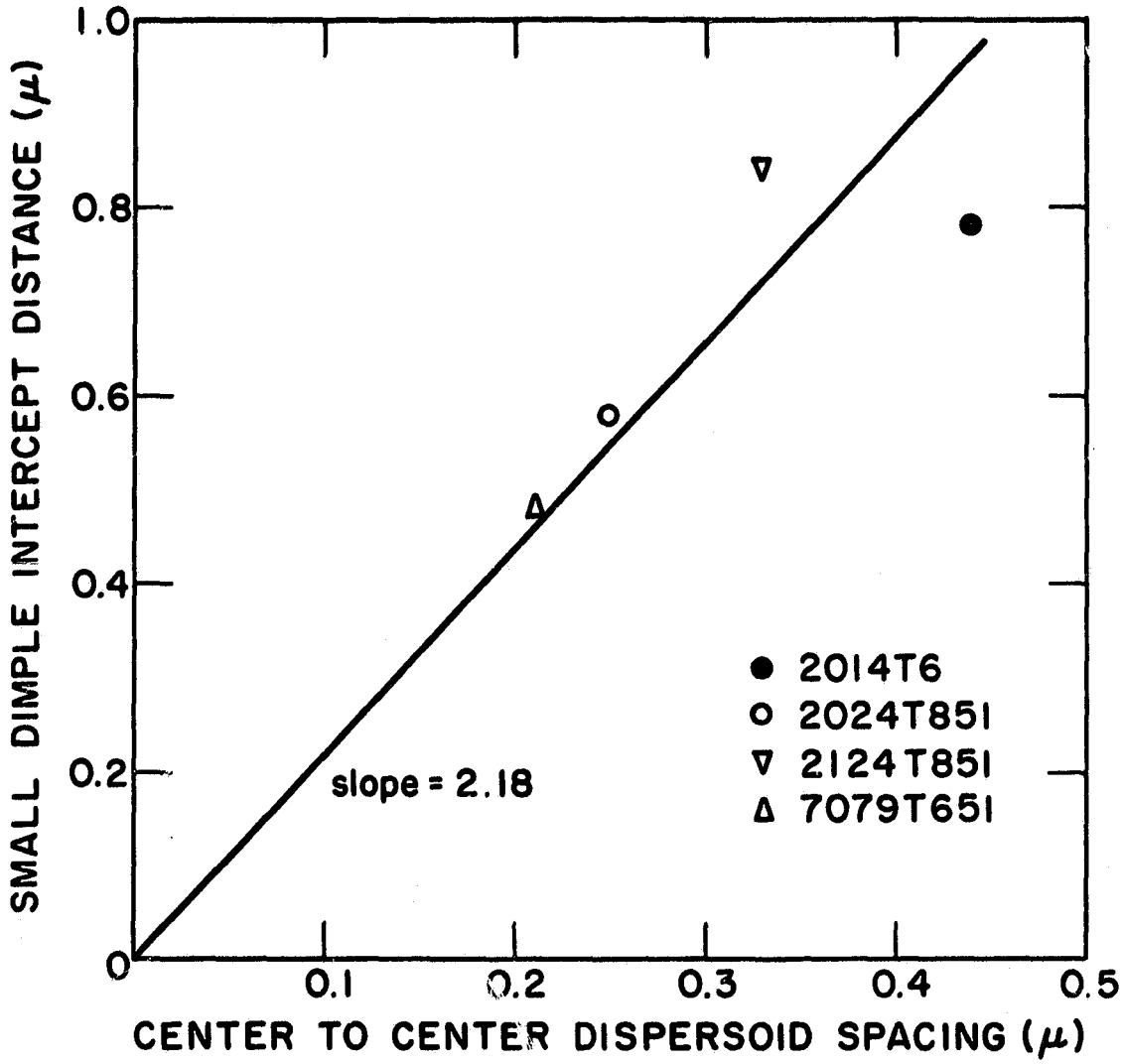

Figure 27 The Center-to-Center Spacing of the Dispersoids as a Function of the Small Dimple Spacing

unity because not every dispersoid acts as a nucleating site for small dimples. In the investigations of Palmer, et.al.[16] and Broek[17], the voids form by interface separation. This is probably the reason that small depressions are often observed in the bottoms of the small dimples indicating the location of the dispersoid-matrix interface. The effect of coalescence on toughness is primarily one of aborting void growth. Dispersoids also act as strengthening particles, so the possible improvement of toughness during the coalescence stage by increasing the dispersoid spacing would diminish the strength.

The stages of void initiation and growth principally control the fracture toughness. The microstructural feature which seems to control both of these is the size and spacing of the second phase particles. As the size of the particles is decreased, void nucleation is retarded, while void growth increases with the particle spacing. Figure 28 shows the K_{Ic} fracture toughness increasing as the spacing between the void nucleating particles becomes greater. Void initiation is apparently retarded by decreasing the particle size as was shown in Figure 24.

The particle spacing is related to the number of particles through equation (1). The number of particles and the particle size determine the volume fraction, and the amount of the second phase in the alloy is determined by the impurity content of the alloy. Thus to appreciably increase the spacing or decrease the size of the second phase particles, the impurity content must be decreased. Figure 29 shows the effect of volume fraction of the void-nucleating phase on K_{Ic} fracture toughness for these alloys.

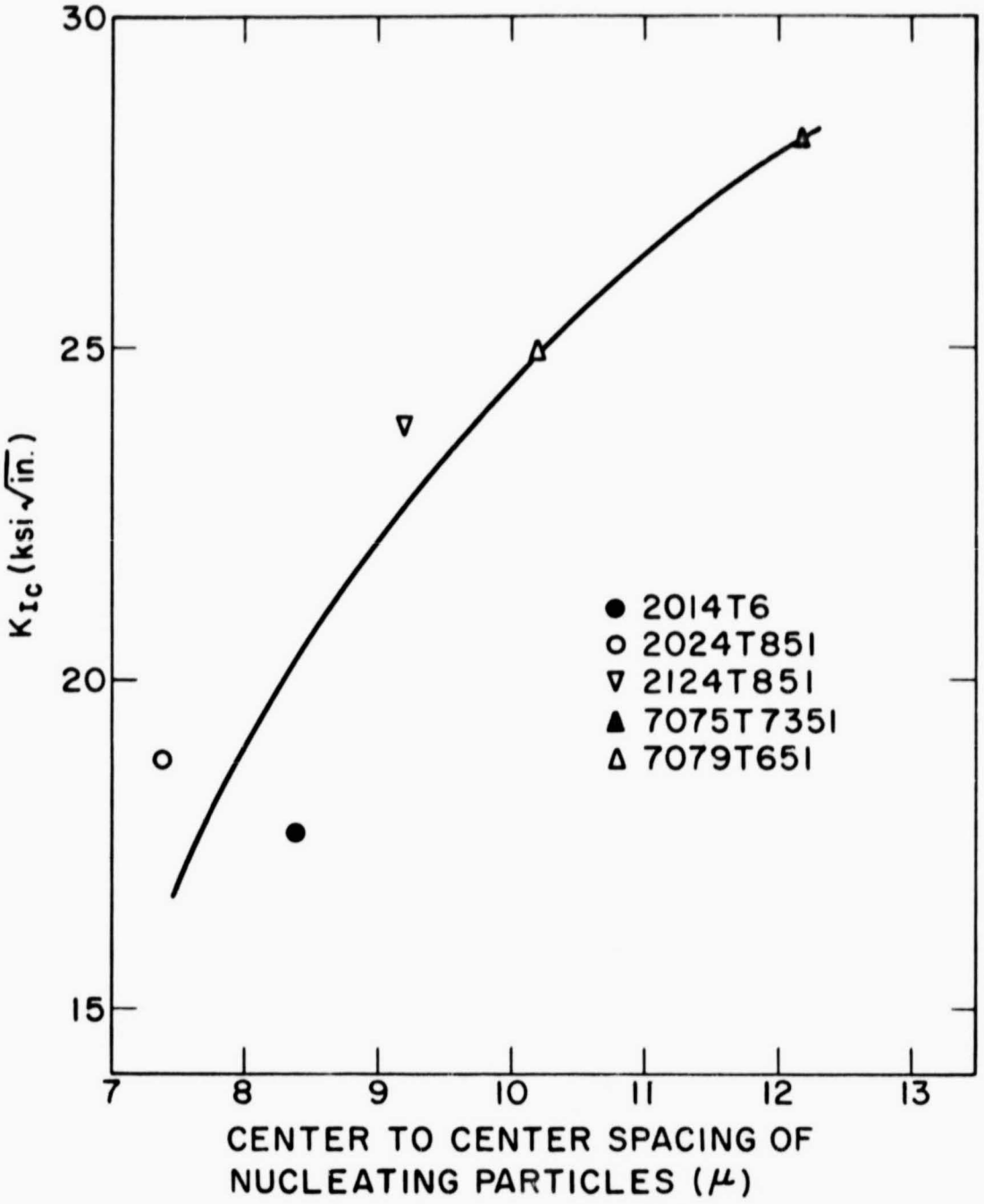

Figure 28 The K_{Ic} Fracture Toughness as a Function of the Center-to-Center Spacing of the Void Nucleating Particles

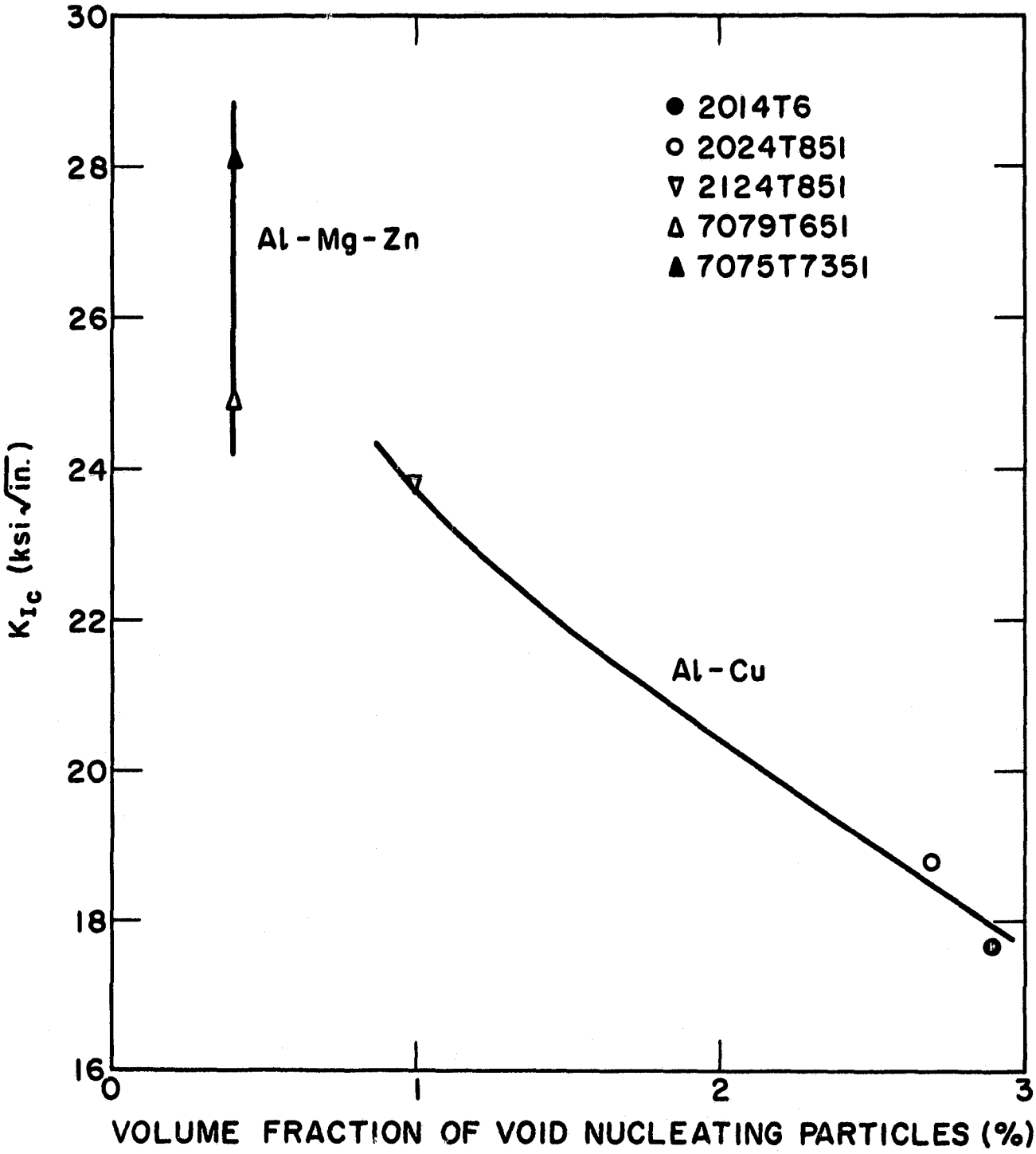

Figure 29 The K_{Ic} Fracture Toughness as a Function of the Volume Fraction of the Second-Phase Particles which Nucleate Voids

The 2000 series alloys have essentially the same yield stress and show improvement in toughness with decreasing volume fraction. The 7000 series alloys have the same volume fraction of second phase particles but have vastly different toughness values. It is not clear if this is due to the difference in yield strength, the play off between particle size and spacing, or if the difference in the composition of the particles causes the difference in cracking behavior as shown in Figure 16.

Additional increases in toughness may be realized by properly balancing the competing size and spacing effects. The five alloys studied here had a very small range of particle size among the void nucleating particles, so the potential of the size effect is not known. Some recent work by Cox and Low[18] on 4340 and 18 Ni-200 grade maraging steels indicates that the size effect may increase toughness more than the spacing effect. In those steels as the impurity level decreases, the inclusions become smaller and more numerous while in the aluminum alloy both the size and number decrease with impurity level. The next stage of this investigation will attempt to assess the contribution and potential of particle size and spacing in aluminum alloys.

In the five alloys studied, the principal impurity elements in the particles are silicon and iron. Although all the particles were observed to crack, those containing iron cracked first and can be considered as the ones which control the toughness. Further work is required to find the effect of the silicon and iron content independently.

Conclusions

1. Fracture toughness in aluminum alloys is principally controlled by the size, spacing, and amount of second phase particles which act as the initiation sites for microscopic voids. The principal impurities in these particles are iron and silicon. The particles containing iron are probably more detrimental to toughness than the silicon-containing particles. The chief method to increase toughness is to decrease the iron and silicon levels.
2. These particles have minor effects on the strength so they act largely to diminish fracture toughness.
3. The void initiation stage is controlled by the size of the void nucleating particles. As the size of the particles decrease, the plastic strain which the particles can withstand prior to cracking increases.
4. Void growth is primarily controlled by the particle spacing. When the spacing is increased, individual voids can grow to a larger size before impinging on neighboring voids. Void growth is apparently stopped when a critical ligament size between adjacent voids is reached, and the coalescence stage intervenes.
5. The void coalescence stage has the smallest effect on toughness and is primarily controlled by sub-micron size dispersoids. Since dispersoids act as strengthening particles, no appreciably increase of toughness can be realized without a corresponding loss in strength.

REFERENCES

1. J. R. Low, Jr., Eng. Frac. Mech., 1, (1968), p. 47.

2. J. Tanaka, C. A. Pampillo and J. R. Low, Jr., NASA Technical Report No. 1, Carnegie-Mellon University, (1969); ASTM STP 463, ASTM Philadelphia, (1970), p. 191.

3. J. G. Kaufman, Alcoa Research Laboratory, Private Communication.

4. J. R. Low, Jr., Prog. Mat. Sci., 12, (1963), p. 1.

5. C. D. Beachem and D. A. Meyn, NRL Memo. 1547, June 1964.

6. H. Y. Hunsicker, W. A. Anderson and W. G. Fricke, Alcoa Research Laboratory, Private Communication.

7. Kent R. VanHorn, Ed., Aluminum, Vol. I, ASM, Metal Park, Ohio.

8. L. F. Mondolfo, Metallurgical Reviews, 16, (1971), p. 95.

9. R. T. DeHoff, Quantitative Microscopy, R. T. DeHoff and F. N. Rhines, Ed., McGraw-Hill, New York, (1968), p. 145.

10. J. Gurland, Quantitative Microscopy, R. T. DeHoff and F. N. Rhines, Ed., McGraw-Hill, New York, (1968), p. 283.

11. John W. Cahn and Jack Nutting, Trans. AIME, 215, (1959), p. 526.

12. A. J. DeArdo, Ph.D. Thesis, Carnegie-Mellon University, (1969).

13. M. S. Hunter and J. C. McMillan, ASTM STP 436, ASTM, Philadelphia, (1968) p. 196.

14. J. Gurland, Trans. AIME, 227, (1963), p. 1146.

15. M. F. Ashby, Phil. Mag., 14, (1966), p. 1157.

16. I. G. Palmer, G. C. Smith and R. D. Warda, Physical Basis of Yield and Fracture, Institute of Physics and Physical Society Conference, Series No. 1, Oxford, England, Sept. 1966.

17. D. Broek, Ph.D. Thesis, Delft Technological University, The Netherlands, (1970).

18. T. B. Cox and J. R. Low, Jr., NASA Technical Report No. 3, Carnegie-Mellon University, May 1972.